1   **No ion is an island:**

2   **Multiple ions influence boron incorporation into CaCO₃**

3

4   *Henehan, Michael J.[a,b*], Klein Gebbinck, Christa D.[c], Wyman, Jillian V. B.[c], Hain, Mathis*

5   *P.[d], Rae, James W. B.[e], Hönisch, Bärbel[f], Foster, Gavin L.[b] and Kim, Sang-Tae[c].*

6

7   [a] Section 3.3 Earth Surface Geochemistry, Deutsches GeoForschungsZentrum GFZ,
8   Telegrafenberg, 14473 Potsdam, Germany.
9   [b] School of Ocean and Earth Science, University of Southampton Waterfront Campus, National
10   Oceanography Centre, Southampton, European Way, Southampton SO14 3ZH, Hampshire, UK.
11   [c] School of Earth, Environment and Society, McMaster University, 1280 Main Street West,
12   Hamilton, ON, L8S 4K1, Canada.
13   [d] Earth and Planetary Sciences Department, University of California Santa Cruz, 1156 High
14   Street, Santa Cruz, CA 95064, USA.
15   [e] School of Earth and Environmental Sciences, University of St Andrews, St Andrews, KY16 9AL,
16   UK.
17   [f] Lamont-Doherty Earth Observatory of Columbia University, Palisades, NY 10964, USA

18

19

20   *Corresponding author: henehan@gfz-potsdam.de

21

22

23

24

25

26

27

28

29

30   **Abstract**

31

32   Boron isotope ratios – as measured in marine calcium carbonate – are an established

33   tracer of past seawater and calcifying fluid pH, and thus a powerful tool for probing marine

34   calcifier physiology and reconstructing past atmospheric CO_2 levels. For such applications,

35   understanding the inorganic baseline upon which foraminiferal vital effects or coral pH

36   upregulation are superimposed should be an important prerequisite. Yet, investigations

37   into boron isotope fractionation in synthetic $CaCO_3$ polymorphs have often reported

38   variable and even conflicting results, implying our understanding of the pathways of boron

39   incorporation into calcium carbonate is incomplete. Here we address this topic with

40   experimental data from synthetic calcite and aragonite precipitated across a range of pH in

41   the presence of both Mg and Ca. We observe coherent patterns in B/Ca and Na/Ca ratios

42   that, we suggest, point to paired substitution of Na and B into the carbonate lattice to

43   achieve local charge balance. In addition, we confirm the results of previous studies that the

44   boron isotope composition of inorganic aragonite precipitates closely reflects that of

45   aqueous borate ion, but that inorganic calcites display a higher degree of scatter, and

46   diverge from the boron isotope composition of aqueous borate ion at low pH. With

47   reference to the simultaneous incorporation of other trace and minor elements, we put

48   forward possible explanations for the observed variability in the concentration and isotopic

49   composition of boron in synthetic $CaCO_3$. In particular, we highlight the potential

50   importance of interface electrostatics in driving variability in our own and published

51   synthetic carbonate datasets. Importantly for palaeo-reconstruction, however, these

52   electrostatic effects are unlikely to play as important a role during natural precipitation of

53   biogenic carbonates.

54

55   KEYWORDS: *Boron Isotopes, Calcite, Aragonite, δ^{11}B, pH proxy, Trace Element Incorporation*

56

57

58   **1. Introduction**

59   The boron isotope-pH proxy, as applied to fossil and modern biogenic carbonates

60   such as foraminifera and corals, is increasingly used to reconstruct both past ocean pH and

61   atmospheric CO_2 levels (e.g. Penman et al., 2014; Martínez-Botí et al., 2015; Anagnostou et

al., 2016; Babila et al., 2018; Henehan et al., 2020) and to provide key insights into the

processes controlling biomineralisation (e.g. McCulloch et al., 2012). Aside from the

demonstrable ability of the proxy to reproduce past CO_2 levels recorded in ice cores (e.g.

Chalk et al., 2017) and its capacity to reconstruct the carbonate chemistry of the calcifying

fluid in stony corals (e.g. Holcomb et al., 2014; Gagnon et al., 2021), its widespread adoption

(at least initially) was fuelled by its strong mechanistic basis, rooted in straightforward

inorganic aqueous geochemistry. This mechanistic basis, and its refinement through time,

is extensively detailed elsewhere (e.g. Hemming and Hanson, 1992; Foster and Rae, 2016;

Rae, 2018; Hönisch et al., 2019), but can be briefly summarised as follows: i) boron dissolved

in seawater speciates primarily between tetrahydroxyborate, or borate ion ($B(OH)_4^-$), and

boric acid ($B(OH)_3$) according to ambient pH, ii) there is a well-defined boron isotope

fractionation associated with this speciation, iii) the charged borate ion is predominantly

incorporated into the $CaCO_3$ crystal structure without isotopic fractionation, and thus iv) the

isotopic composition (and perhaps concentration) of boron in carbonates should reflect the

changing isotopic composition (and abundance) of aqueous borate ion with changing

seawater pH. While this conceptual basis was initially supported by the similarity of the $\delta^{11}B$

of marine biogenic carbonates to that of borate ion (Hemming and Hanson, 1992),

subsequent research has found that while the $\delta^{11}B$ of experimentally-precipitated synthetic

aragonite does closely match that of aqueous borate ion (Noireaux et al., 2015), no synthetic

calcites precipitated to date (Sanyal et al., 2000; Noireaux et al., 2015; Kaczmarek et al., 2016a;

Farmer et al., 2019) show as high a sensitivity of $\delta^{11}B$ to pH as would be predicted for

aqueous borate ion using current estimates of the isotope fractionation between aqueous

borate ion and boric acid (Klochko et al., 2006; Nir et al., 2015). Further, inorganically-

precipitated calcite tends to mainly, but not exclusively (e.g see datapoint classified as an

outlier by Noireaux et al., 2015) record $\delta^{11}B$ that is higher than the $\delta^{11}B$ of ambient borate

ion ($\delta^{11}B_{borate}$). While deviations from the aqueous conceptual basis of the proxy in biogenic

88   carbonates can often be attributed to physiological processes that decouple chemical

89   conditions of $CaCO_3$ precipitation from bulk seawater chemistry, such as variable pH up-

90   regulation in corals (e.g. Venn et al., 2013) or microenvironment alteration in foraminifera

91   (e.g. Hönisch et al., 2003), inorganically-precipitated $CaCO_3$ is not subject to such vital effects,

92   and as such the variability of results from synthetic carbonates challenges our current

93   understanding. Furthermore, the reason why boron isotope incorporation behaviour should

94   be so strongly dependent on polymorph is not fully understood.

95   One potential mechanism by which inorganic carbonates may be elevated relative

96   to ambient borate ion is the incorporation of some amount of boric acid (which is

97   isotopically heavier than borate ion). Since the isotopic fractionation between boric acid and

98   borate ion is large (~26-27.2‰; Klochko et al., 2006; Nir et al., 2015), any potential

99   contribution from boric acid in ancient calcites that was non-systematic would impede

100   attempts to resolve past changes in ocean pH using the boron isotope composition of

101   marine carbonate. Incorporation of both aqueous boron species has often been inferred

102   based on nuclear magnetic resonance (NMR) studies showing boron in carbonates may be

103   trigonally or tetrahedrally coordinated (e.g. Sen et al., 1994; Klochko et al., 2009; Mavromatis

104   et al., 2015; Noireaux et al., 2015). Since aqueous boric acid is trigonally-coordinated, some

105   have cited this trigonal coordination in carbonate as evidence of boric acid inclusion (e.g.

106   Klochko et al., 2009; Cusack et al., 2015; Noireaux et al., 2015; Balan et al., 2016). However,

107   the proportion of trigonal boron observed in carbonates correlates very poorly with

108   measured elevation of $\delta^{11}B$ relative to borate ion (Branson et al., 2015; Noireaux et al., 2015),

109   cautioning against directly equating NMR coordination to the original aqueous boron

110   species that was incorporated (see also Sen et al., 1994).

111   An alternative line of argument for inclusion of both aqueous species in calcite

112   comes from improved goodness-of-fit in observed synthetic calcites (but not aragonites;

113   Holcomb et al., 2016) when boron partitioning is parameterised by λ_B ($\lambda_B = B/Ca_{carbonate}$ /

114   ([B]$_{solution}$/[Dissolved Inorganic Carbon]$_{solution}$)) rather than via aqueous borate concentration

115   alone (e.g. Uchikawa et al., 2015). Indeed, Branson (2018), and subsequently Farmer et al.

116   (2019), have had considerable success in explaining some (but not all) published boron

117   isotope data from synthetic carbonates within a surface kinetic modelling (SKM) framework

118   (building on DePaolo, 2011), involving both major aqueous boron species. In this model, the

119   boron isotope composition of the precipitated mineral is determined by the balance

120   between detachment and attachment rates of either species to the growing crystal face.

121   Differences in boron isotope composition between experimental calcites and aragonites

122   can thus be explained via a slower detachment rate of trigonal boric acid from the growing

123   calcite face, and thus a greater propensity for retention of this isotopically-heavy species in

124   the crystal lattice. This model can explain variability across the wide range of experimental

125   treatments (pH, [DIC], [Ca^{2+}], and [B]) of Uchikawa et al. (2015; 2017), as well as much, if not

126   all, published data from elsewhere (Mavromatis et al., 2015; Noireaux et al., 2015; Kaczmarek

127   et al., 2016a). While the SKM approach clearly appears to be very promising, there are

128   outstanding questions that would benefit from the provision of more experimental data.

129   For instance, it is not yet possible to conclusively distinguish whether published data are

130   better explained via the Surface Entrapment Model (SEMO, where impurities in a surface

131   boundary layer are trapped by rapid crystal overgrowth; Watson, 2004) or the SKM model.

132   Also, intriguingly, structure in the residuals between SKM model predictions and

133   experimental observations points to the existence of an as-yet-unidentified process that is

134   not parameterised in the model, perhaps linked to a secondary control on the availability of

135   binding sites (Farmer et al., 2019). Additionally, adsorption experiments by Saldi et al. (2018)

136   found little support for adsorption of trigonally coordinated boric acid to the calcite surface,

137   which would make it difficult to envisage attachment rates of boric acid ever exceeding

138   those of detachment, as the SKM would require. More fundamentally perhaps, the observed

139   isotopic fractionations during adsorption of borate ion (Saldi et al., 2018) and modelled

140 equilibrium fractionation between the solid carbonate and aqueous boron phases (Balan et

141 al., 2016; Balan et al., 2018) call into question some of the fundamental assumptions of the

142 SKM model and indeed of the boron isotope proxy in general.

143   To address these outstanding questions, we present new $\delta^{11}B$ data from experimentally-

144 precipitated synthetic calcite and aragonite, measured via multicollector inductively-

145 coupled plasma mass spectrometry (MC-ICPMS). These precipitates, grown without seed

146 material at seawater-like ionic strength (I = 0.7 mol/kg) in the presence of Mg, expand the

147 range of pH (~7.4 – 9.4) covered by previous published data. Careful monitoring of the

148 oxygen isotope compositions of precipitates and parent water show they were formed at

149 (or close to) oxygen isotope equilibrium with parent water (see Kim et al., 2014). Since B

150 isotopic equilibrium is reached before O isotope equilibrium (Zeebe et al., 2001), a lack of

151 non-equilibrium isotope effects for O isotopes should suggest a corresponding lack for B.

152 Boron isotope measurements are coupled with measurements of other trace and minor

153 element-Ca ratios, to place observed isotopic fractionations within a broader framework

154 that also considers other interacting and/or competing ions. Finally, we also include the

155 results of a reanalysis of the calcite precipitates of Sanyal et al. (2000) via MC-ICPMS, allowing

156 greater ease of comparison with newer data, without necessitating consideration of

157 possible analytical offsets in negative thermal ionisation mass spectrometry (NTIMS) data

158 (e.g. Hönisch et al., 2003; Foster et al., 2013; Farmer et al., 2016).

159

160 **2. Methods**

161 **2.1 CaCO$_3$ precipitation via the Constant Addition Method**

162   Methodology for calcite or aragonite precipitation largely followed Kim et al. (2014),

163 with the addition of B ([B]= 7.9 mmol/kgw) in the growth medium. Starting experimental

164 solutions for CaCO$_3$ precipitation experiments were prepared gravimetrically using

165 deionized water (18.2 MΩ cm) and ACS grade B(OH)$_3$, NaCl and NaHCO$_3$ and/or Na$_2$CO$_3$,

166 dependent on the intended starting pH of the experimental solution (all at $I =\sim 0.7$

167 mol/kgw). To ensure oxygen isotope equilibrium between the DIC species and water,

168 solutions were left to equilibrate for a minimum of 7 days in a temperature-controlled water

169 bath at $25 \pm 0.01°C$. Immediately prior to beginning each synthesis experiment, ACS grade

170 $MgCl_2 \cdot 6H_2O$ and $CaCl_2 \cdot 2H_2O$ were added to these isotopically-equilibrated starting solutions

171 (see Table 1 for details). The ratio of [Mg] to [Ca] differed according to the desired polymorph

172 in each experiment (Morse et al., 2007): aragonite was precipitated at a solution Mg:Ca of

173 4:1, but in order to precipitate calcite, solution Mg:Ca was lowered to 0.13:1. The addition of

174 the hydrated chloride salts had no detectable influence on the oxygen isotopic composition

175 of the growth medium, due to their relatively low concentrations. Starting solutions were

176 then held in an airtight Teflon reaction chamber at 25.04 ± 0.03 °C (aragonite) or 25.00 ± 0.04

177 °C (calcite).

178   Precipitation of $CaCO_3$ began with the constant addition of two titrants (also of $I = 0.7$

179 mol/kgw), the first a NaCl and $NaHCO_3$ and/or Na_2CO_3 solution, the second a $CaCl_2 \cdot 2H_2O$,

180 $B(OH)_3$, and NaCl solution (see Table 1). Both were prepared with deionized water from the

181 same batch as that used in the starting solution to ensure consistency of $\delta^{18}O_{H2O}$. After

182 nucleation, which is spontaneous and involves no seed material, precipitation rate and

183 solution pH were paced by the steady rate of injection of two titrants (at 0.5 ml hr^{-1}). Because

184 these experiments were carried out in sealed reaction vessels without a Ca electrode, exact

185 timing of nucleation is not known. Based on prior experience during the development of

186 the constant addition method (Kim et al., 2006; Kim et al., 2014), however, nucleation occurs

187 soon after titration begins (at latest 24-48 hours). The composition of titrants was designed

188 to keep pH stable during precipitation experiments, but where adjustments were necessary,

189 1% HCl was added. Precipitation lasted between 67 and 627 hours from the onset of

190 titration, depending on the experiment, yielding between 42 and 389 mg of $CaCO_3$ (Table

191 1). The pH of the growth medium was measured daily, using an NBS-calibrated

192   potentiometric electrode. Within-run pH variability for experiments at medium-range pHs

193   (~ 8.5 - 9) was often less than 0.1 pH units (at 2 sd), but was considerably larger for some low-

194   pH experiments (up to 0.28 units, 2sd), as shown in Supp. Fig. 1. However, since this

195   variability during the experiment is averaged out in the carbonate sample that is ultimately

196   analysed, we take two standard error on the mean pH as our uncertainty. Note, for input to

197   PHREEQC, these NBS pH values were converted to MacInnes convention pH (Nir et al., 2014).

198   Aliquots of the growth medium were taken for boron and oxygen isotope analysis at the

199   beginning and end of each precipitation experiment, with samples for boron filtered

200   through a 0.45 μm Millipore Durapore® syringe filter to remove any suspended crystalline

201   material, and subsequently stored in acid-cleaned high-density polyethylene bottles. Upon

202   collection of water samples, the remaining precipitation medium was run through a vacuum

203   filtration system using 0.45 μm Durapore® membrane filters to isolate the suspended

204   crystals. These were thoroughly rinsed with 2 L of 18.2 MΩ Milli-Q water to remove residue

205   from the growth media, followed by ultra-pure methanol to remove water that might later

206   interact with the carbonate, and oven-dried at ~ 70 °C overnight before weighing.

207   Mineralogy of samples was screened using X-ray diffraction (XRD), with all experimental

208   carbonates analysed here (with the possible exception of sample iMH15) found to consist of

209   purely one polymorph (at least within the resolution of the technique). All measured XRD

210   spectra are provided in Supplementary Appendix 2.

211   **2.2 Oxygen isotope analysis**

212   Oxygen isotope compositions of calcium carbonate samples were determined using a

213   VG OPTIMA isotope ratio mass spectrometer at McMaster University, equipped with an

214   ISOCARB automated common acid bath at 90 °C, with a 1σ uncertainty on $\delta^{18}O$

215   measurements of ± 0.08 ‰. The measured $\delta^{18}O$ values of acid-liberated CO_2 ($\delta^{18}O_{CO2(ACID)}$)

216   from two reference materials (NBS 18 and NBS 19) at 90 °C were fitted against the $\delta^{18}O_{CO2(ACID)}$

217   value of 17.48 ‰ (NBS 18) and 39.19 ‰ (NBS 19). The measured $\delta^{18}O_{CO2(ACID)}$ value from each

218   sample was then normalized using the relationship obtained above, and the acid

219   fractionation factor of 1.0163 for aragonite or 1.01030 for calcite at 25 °C (Kim et al., 2007)

220   was used to calculate the oxygen isotope composition of synthetic aragonite ($\delta^{18}O_{Aragontie}$) or

221   calcite ($\delta^{18}O_{Calcite}$).

222   For oxygen isotope analysis of water samples, a modified CO_2-H_2O equilibration

223   technique (Epstein and Mayeda, 1953) was employed using a Gas Bench II headspace

224   autosampler and a Thermo Finnigan DeltaPlus XP Isotope Ratio Mass Spectrometer (IRMS)

225   at McMaster University. Exetainer® glass vials were flushed and filled with a 0.2% CO_2 and

226   99.8% He mixture with a double needle at a flow of 100 ml min^{-1}. 0.2 ml of water sample was

227   injected into each glass vial, allowing ≥27 hr to equilibrate at 25 ±0.1 °C before the CO_2 in

228   the headspace was analyzed by IRMS. Samples were analyzed in duplicate with in-house

229   water standards MRSI-STD-W1 and MRSI-STD-W2 ($\delta^{18}O$ = -0.58 ‰ and -28.08 ‰

230   respectively). Uncertainty on water $\delta^{18}O$ measurements is ± 0.05 ‰ (1σ).

231   **2.3 Boron isotope analysis**

232   All boron isotope analyses were carried out at the University of Southampton (UoS),

233   using multi-collector inductively-coupled plasma mass spectrometry (MC-ICPMS), following

234   Foster (2008) and Henehan et al. (2013). As is critical for inorganic precipitation experiments

235   such as these, sample precipitates were cleaned thoroughly to ensure complete removal of

236   any boron that may have adhered to the mineral surface from the experimental medium.

237   Specifically, having been rinsed with 2 L of MilliQ water before drying and transportation,

238   carbonate samples were then rinsed five times with ~500 μL of boron- free MilliQ water,

239   ultrasonicated (30 s) and centrifuged (4 mins). Each time, supernatant was extracted,

240   acidified, and analysed for B/Ca on a Thermo X-Series II Quadropole ICPMS to verify the

241   efficiency of rinsing, and to ensure the analysed carbonate was free of adsorbed B (see Supp.

242   Fig. 2). Carbonate samples were then transferred to Teflon centrifuge tubes, subjected to a

243   weak acid leach (0.0005M HNO_3) to remove any adsorbed contaminants, rinsed three times

244   more to remove the weak acid, and finally dissolved via stepwise addition of 0.5M HNO_3. For

245   each sample, a 20 μl aliquot of dissolved material was taken for trace and minor element/Ca

246   ratio analysis (see Section 2.4). Samples of the experimental medium were acidified with

247   HNO_3 and ultrasonicated prior to analysis to ensure any possible precipitates were

248   redissolved. Subsequently, separation of B from matrix prior to analysis via ion

249   chromatography followed Henehan et al. (2013).

250   Analytical uncertainty was estimated with reference to repeat analyses of JCp-1 coral

251   aragonite standard (Okai et al., 2002) measured at UoS on 10^{11} Ω amplifiers, using the

252   relationship between 2σ external reproducibility and [11]B signal intensity from Henehan et

253   al. (2013). Typical long-term reproducibility was < 0.23‰ (2sd) for 20 ng B and < 0.33‰

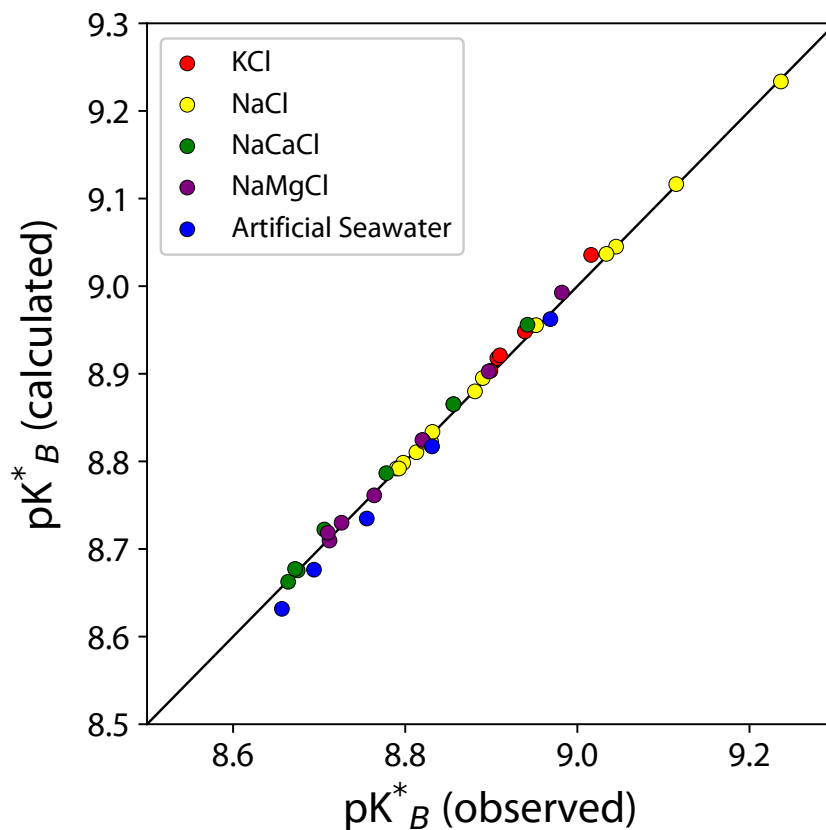254   (2sd) for 4 ng B.

255   **2.4 Trace and Minor Element/Ca ratios**

256   Trace and minor element/Ca ratios were measured on an aliquot of the same dissolved

257   sample material as was analysed for boron isotope ratios, using a Thermo Element ICP-MS

258   at UoS. Measurement methods are detailed in Henehan et al. (2015). Reproducibility of

259   element/Ca ratio measurements was gauged by repeat measurement of three in-house

260   consistency standards (B/Ca ratios of 197, 496, and 32 μmol/mol, respectively) with these

261   sample runs, and was 6% for B/Ca, 1% for Na/Ca and 2% for Mg/Ca (all at 2 sd).

262   **2.5 Aqueous boron and carbonate speciation calculations**

263   Since the parameterization of pK^*_B (the equilibrium constant between boric acid and

264   borate ion in solution) typically used in boron isotope-pH reconstructions (Dickson, 1990a)

265   is based on 'normal' seawater chemistry, it is not applicable to the Na-Ca-Mg-Cl solutions

266   used here. Approaches taken to address this issue in previous studies have varied and may

267   contribute to the variability observed between studies. Kaczmarek et al. (2016a) and

268   Noireaux et al. (2015) used the MINTEQA2 database, within the framework of PHREEQC

269   (Parkhurst and Appelo, 2013) to calculate aqueous speciation. While this database uses the

270   Davies equations (Davies, 1938) to extend Debye–Hückel parameters to higher ionic

271   strengths than their original derivations, these equations are still not intended for use at

272   ionic strengths greater than ~ 0.5 M. Consequently, while for the low ionic strength growth

273   media (0.1 - 0.2 M) of Noireaux et al. this should not introduce significant error, for the higher

274   ionic strength experiments of Kaczmarek et al. this database is not suitable. The MyAMI

275   model (Hain et al., 2015), itself developed from the MIAMI Ionic Interaction Model (Millero

276   and Pierrot, 1998), can be used to calculate pK^*_B and carbonate equilibrium constants for

277   palaeo-seawater with different [Ca] and [Mg], but at unusual ionic strengths and solution

278   chemistries far removed from seawater it produces values of pK^*_B that diverge significantly

279   from experimentally determined values (Farmer et al., 2019). Instead, Farmer et al. (2019)

280   used the Pitzer database (pitzer.dat) implemented within PHREEQC (Parkhurst and Appelo,

281   2013) because the output pK^*_B values best fit measured observations across a range of

282   experimental solution chemistries, notwithstanding some divergences between calculated

283   and observed pK^*_B values in artificial seawater. Following these authors, we also use the

284   Pitzer database here, but we note that when one accounts for the fact that empirical artificial

285   seawater pK^*_B values (Dickson, 1990a) are reported on the total scale, and calculation of pK^*_B

286   from speciation in PHREEQC is based on the free scale (or more specifically, MacInnes

287   convention pH; Nir et al., 2014), the fit between Pitzer-calculated pK^*_B and empirical pK^*_B (Fig.

288   1) is in fact even better than was reported by Farmer et al. (2019).

Figure 1: Values of pK*_B calculated by the Pitzer database within PHREEQC (Parkhurst and Appelo, 2013) agree well with empirical observations across a broad range of ionic strengths (0 - 6.15 M) in KCl solutions (Dickson, 1990b), NaCl solutions (Owen and King, 1943; Hershey et al., 1986), Na-Mg-Cl and Na-Ca-Cl solutions (Hershey et al., 1986), and even artificial seawater, once corrected from total scale (Dickson, 1990a). Since our solution chemistries (Na-Mg-Ca-B-Cl) are intermediate between those of Hershey et al. (1986) and Dickson (1990a), the Pitzer database can be considered appropriate for use here, as well as in recalculation of published data.

Our speciation calculations use concentrations of ions in precipitation media, as determined both from gravimetric measurements of starting reagents and titrants, and from gravimetric (mass of dried $CaCO_3$) and geochemical (from measured Na/Ca, B/Ca and Mg/Ca ratios in $CaCO_3$) quantification of ions removed in precipitates over the course of the experiments. These concentrations are given in Supplementary Table 1. Although the concentrations of some ions (e.g. Na, B) varied somewhat through each of our precipitation experiments, the resultant change in $\delta^{11}B_{borate}$ due to these variations was less than 0.1 ‰. Nonetheless for our study and for the study of Kaczmarek et al. (2016a) we incorporate uncertainty in calculated pK*_B and Saturation Index (SI; SI = log_{10}((Ionic Activity Product)/(Polymorph solubility constant K_{sp})) due to changing major ion concentrations,

306   along with variability in growth medium pH and uncertainty in growth medium $\delta^{11}B$, via a

307   Monte Carlo approach. Specifically, 2,000 simulated datasets were generated within a

308   uniform distribution between starting major ion concentrations and their corresponding

309   concentrations at the end of each experiment (accounting for solute loss into the

310   precipitates), and from normal distributions within pH and $\delta^{11}B_{solution}$ uncertainty. Speciation

311   was then calculated for each Monte Carlo solution using the PhreeqPy implementation of

312   PHREEQC in Python (https://phreeqpy.com), which is in turn facilitated by IPhreeqc

313   (Charlton and Parkhurst, 2011a), and boron isotope calculations calculated with reference

314   to absolute isotope ratios (Rae, 2018) using modified formulations of code used by Farmer

315   et al. (2019) and made available by O. Branson (https://github.com/oscarbranson).

316

317   **2.6 Quantifying precipitation rate**

318   Published experimental data (Uchikawa et al., 2015; Kaczmarek et al., 2016a; Uchikawa

319   et al., 2017) have highlighted the importance of precipitation rate (R) in controlling boron

320   incorporation. While we have no Brunauer–Emmett–Teller (BET)-based estimate of surface-

321   area normalised precipitation rate for our experiments, we can calculate a number of other

322   (albeit imperfect) indicators of precipitation rate that can be compared to geochemical

323   results. Amongst these, estimates of bulk precipitation rate (i.e., mass of carbonate

324   precipitated per hour) should be most indicative of the crystal-scale growth rate, even if

325   other factors relating to crystal form likely make this an imperfect proxy. Indeed, in studies

326   where area-normalised precipitation rate is available, this correlates reasonably well with

327   the bulk precipitation rate metric we use here (Supp. Fig. 3). Other possible indicators of

328   crystal-scale growth rate include SI, which should strongly influence precipitation rate

329   (Zhang and Nancollas, 1998). However, since in our experiments growth medium Mg

330   concentrations varied, potentially variable retardation effects on (particularly calcite) crystal

331   growth (e.g. Berner, 1975; Nielsen et al., 2016) between experiments mean using SI as a

332   proxy for precipitation rate may also not be straightforward. Indeed, we note that for our

333   experiments, precipitation rate in mg hr^{-1} is negatively correlated with pH and SI (Supp. Fig.

334   4). For this same reason, it is not possible to use the relationship between observed R and SI

335   from Uchikawa et al. (2015; 2017) to estimate surface area-normalised growth rate following

336   Farmer et al. (2019), as their experimental solutions did not contain Mg. Furthermore, their

337   relationship based on calcite precipitation experiments is likely not applicable to our

338   aragonites. Alternatively, others have noted the influence of $[Ca^{2+}]/[CO_3^{2-}]$ as a primary

339   control on calcite growth rate when saturation is otherwise held roughly constant (Nehrke

340   et al., 2007; van der Weijden and van der Weijden, 2014), and ability of the $CaCO_3$

341   product/sum ratio to predict growth rate of Mg-rich amorphous $CaCO_3$ (ACC) when Ω varies

342   (Evans et al., 2020) and so we consider these here as other possible indicators of crystal

343   growth rates in our experiments (noting that both correlate well with bulk precipitation rate,

344   our preferred metric; Supp. Fig. 5).

345

346   **2.7 Reanalysis of Sanyal et al. (2000) carbonates**

347   For information regarding the precipitation experiments of Sanyal et al. (2000), we refer

348   the reader to the original publication. Although not stated by Sanyal et al. (2000), the

349   artificial seawater used in their study followed the recipe of Kester et al. (1967), but with the

350   omission of Mg, and some alteration of [Ca] to moderate precipitation rates (J. Bijma, pers.

351   comm.). Records of the exact values of [Ca] are no longer available, and thus in the absence

352   of better estimates we assume seawater [Ca] in speciation calculations here, with the proviso

353   that these values are likely inaccurate. MC-ICPMS and ICPMS analyses were carried out at the

354   University of Bristol, following the methods of Foster (2008), and with uncertainty on these

355   data being two standard deviations of four replicate measurements. B/Ca ratios in the first

356   three rinse steps were measured to assess efficacy of cleaning, before a subsequent weak

357   acid leach and three further Milli-Q leaches. While after three rinses B/Ca ratios in the rinse

358   solutions levelled off somewhat, we cannot be certain that these rinses were sufficient (see

359   Supplementary Appendix A for full discussion). Hence, given this uncertainty, and that

360   surrounding [Ca] in the growth media, we refrain from over-interpreting these data in this

361   study.

362

363   **3   Results**

364   **3.1 Experimental conditions and equilibrium fractionation**

365   Details of conditions during each precipitation experiment, along with masses of

366   resultant precipitate and precipitation rates, are given in Table 1. For further details of the

367   evolution of growth medium chemistry, see the Supplementary Table 1. Precipitation rates

368   based on total mass precipitated range from 0.11 to 1.58 mg/hr for aragonites, and 0.15 to

369   0.73 mg/hr for calcites. The observed oxygen isotope fractionation of synthetic aragonites

370   ($1000\ln\alpha_{aragonite-water}$) ranges between 28.80 and 29.15 ‰ (Table 2), within analytical

371   uncertainty of the published estimate of 28.87 ± 0.13 ‰ at the same ionic strength of $I =$

372   ~0.7 mol/kg reported by Kim et al. (2014). Calcite samples are however systematically offset

373   by ~ 0.5 - 0.7 ‰ (i.e. beyond combined 2σ analytical uncertainty of 0.19 ‰) from the

374   equilibrium calcite-water fractionation proposed by Kim and O'Neil (1997) using not only a

375   different technique of carbonate precipitation – where supersaturation of the precipitation

376   medium was reached by bubbling N_2 gas to forcibly degas CO_2 – but also a much lower ionic

377   strength. This offset is not strongly correlated with pH or SI, or [Ca]/[DIC] in either aragonite

378   or calcite precipitation experiments (see Supp. Fig. 6).

379

380   **3.2 Trace element ratios**

381   Minor (Na, Mg, Sr) and trace (B, Mn, Cd, Ba, U, Nd, Al) element-Ca ratios are listed in Table

382   2 and Supplementary Table 2. Note however that of these elements, only Na, Mg, and B were

383   intentionally and quantifiably added to the growth media; other elements could only have

384   been introduced as impurities in original reagents, or via contamination from experimental

385   apparatus. We provide these data in the supplement for posterity, but since it is inadvisable

386   to over-interpret the distribution of elements whose concentrations in the experimental

387   fluid were not controlled, we do not discuss these further. Observed Na/Ca ratios in

388   aragonites ranged from 9 – 32 mmol/mol, compared to only 2 – 8 mmol/mol in calcites,

389   confirming a higher affinity for Na in aragonite observed elsewhere (Kitano et al., 1975). B/Ca

390   ratios are also similarly higher in aragonite (350 - 1852 µmol/mol) than calcite (107 – 315

391   µmol/mol), in agreement with previous studies (e.g. Furst et al., 1976; Kitano et al., 1978;

392   Noireaux et al., 2015). Conversely, despite higher aqueous [Mg] in aragonite growth media,

393   Mg/Ca ratios were often higher in calcites (2.6 - 5.1 mmol/mol) than aragonites (0.9 – 6.0

394   mmol/mol), as observed elsewhere (e.g. Berner, 1975).

395   B/Ca ratios (Fig. 2a) and elemental partitioning (expressed here as λ_B, defined above, Fig

396   2b) are significantly positively linearly correlated with experimental pH for both aragonite

397   ($R^2_{B/Ca}$ = 0.29, $R^2_{\lambda B}$ = 0.39) and calcite ($R^2_{B/Ca}$ = 0.74, $R^2_{\lambda B}$ = 0.73). Na/Ca ratios are similarly

398   positively correlated with pH (Fig. 2d) in both aragonite ($R^2_{Na/Ca}$ = 0.67) and calcite ($R^2_{Na/Ca}$ =

399   0.93). However, when one accounts for the considerable range in growth medium Na/Ca,

400   partitioning of Na (i.e. $D_{Element}$: Element/Ca$_{solid}$ / Element/Ca$_{solution}$) into the solid form is in fact

401   lower when pH is higher (Fig. 2e). Mg/Ca (Fig. 2g) shows little response to pH in calcites, but

402   when changing solution [Mg] between experiments is accounted for (D_{Mg}; Fig 2h, i), there is

403   an evident increase in Mg partitioning into aragonite at higher pH/SI. Because in our

404   experiments calculated SI was linearly correlated with pH (R^2_{calc} = 0.60, p_{calc} = 0.01; R^2_{arag}=0.50,

405   p_{arag} < 0.01; Supp. Fig. 7), similar trends for each element are seen against SI (Fig 2 c, f, i),

406   although in most cases the correlations are weaker than for pH.

● Calcites, this study   ■ Aragonites, this study
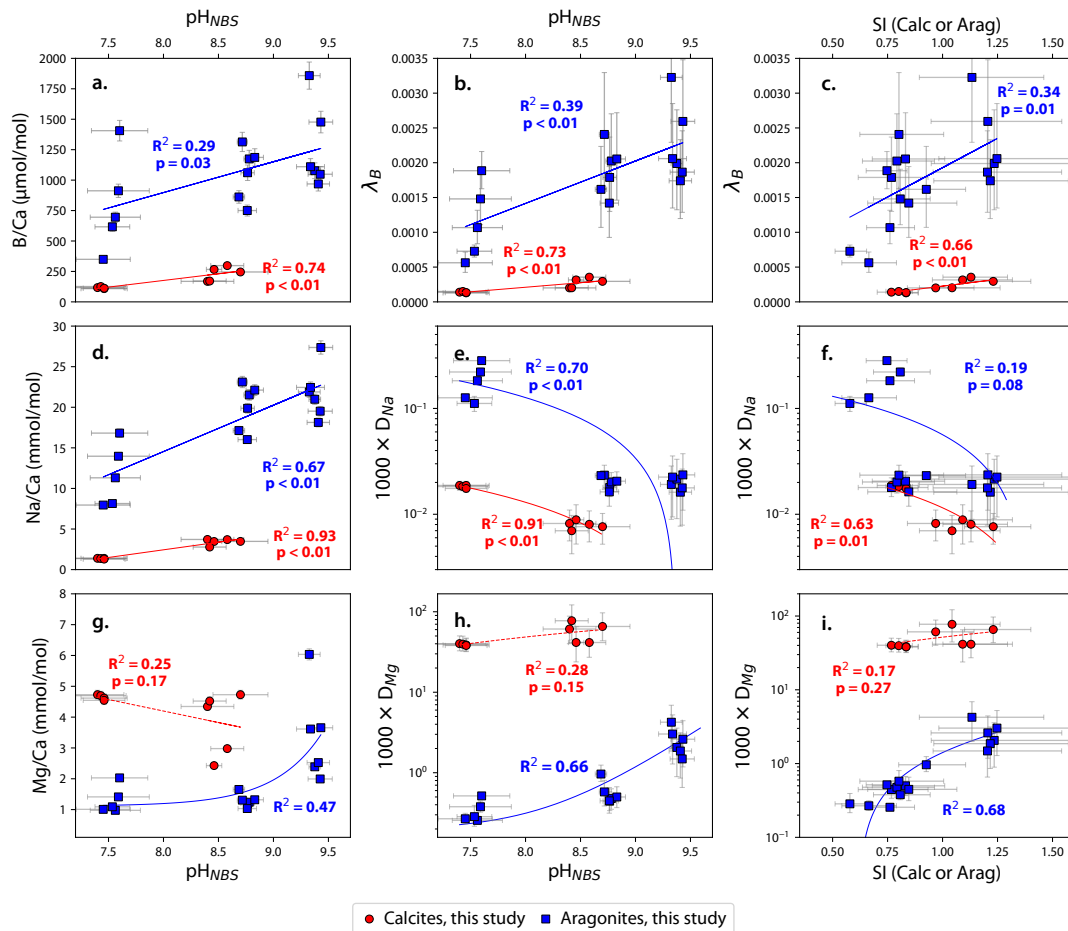
Figure 2: The observed response of B, Na and Mg incorporation to changes in the carbonate system. Both B/Ca (panel a) and Na/Ca (panel d) ratios increase with pH in both aragonites (blue squares) and calcites (red circles). Because B/DIC did not vary significantly in the experiments, this is equally evident in λ_B values ($\lambda_B = B/Ca_{carbonate} / ([B]_{solution}/[DIC]_{solution})$), shown in panel e. By contrast, because Na/Ca ratios in the growth medium vary considerably, pH appears to promote Na incorporation when plotted as raw Na/Ca ratios (panel d), but in fact partitioning of Na into the solid form (D_{Na}) is lower when pH is higher (panel e). Regression fits shown are based on the median slope and intercept of 2000 Monte Carlo datasets sampled within normal distributions of uncertainty around x and y variables, and stated statistics are the median R^2 and p-values of these Monte Carlo fits. The aragonite fits in panels g-i are exceptions to this: these are least-squares exponential fits through the central tendencies of the data, as linear fits resulted in considerably worse goodness-of-fit. For these fits, meaningful p-values could not be calculated. The form of regression fit applied was chosen to maximise R^2. See Supp. Fig 8 for panel h plotted on a linear scale, and Supp. Fig. 9 for a version of this Figure also including remeasured values of calcites from Sanyal et al. (2000).

While these relationships highlight the predominant control of the carbonate system on boron incorporation, there is clearly considerable residual variability around these relationships, with individual aragonite precipitate B/Ca values varying by ~1000 µmol/mol even within very similar low pH treatments. Note that the strength of the carbonate system

427 control on B/Ca is not any more significant when plotted against calculated $[B(OH)_4^-]/[HCO_3^-$

428 $]$, $[B(OH)_4^-]/[DIC]$ or $[B(OH)_4^-]/[CO_3^{2-}]^{0.5}$, and so we plot against pH as the least derived (and

429 hence least uncertain) parameter here (see Supp. Fig. 10 for alternative parameterisations).

430 Similarly, we cannot discern whether there is any better fit between λ_B (plotted here

431 following Uchikawa et al. (2015)) or $[B(OH)_4^-]/[DIC]$, although it is perhaps notable that our

432 calcites and those remeasured values of Sanyal et al. (2000) fall on a similar trend when

433 $[B(OH)_4^-]/[DIC]$ is used (Supp. Fig. 10). Given published experimental data point to

434 precipitation rate (R) being important in controlling boron incorporation

435 (Uchikawa et al., 2015; Kaczmarek et al., 2016a; Uchikawa et al., 2017), one might predict

436 residual variation from a relationship with the carbonate system in our experiments to be

437 correlated with precipitation rate. Despite this, although our metrics for precipitation rate

438 (bulk precipitation rate, SI, or $[Ca]/[CO_3^{2-}]$) may be imperfect substitutes for BET-based

439 surface-area normalised precipitation rate (as we discuss in Section 2.6), it is striking that

440 there is no correlation between *any* of these growth-rate metrics and residual variability

441 from our observed B/Ca-pH relationship (Fig. 3a-d). Neither is there any correlation with the

442 ratio of growth-inhibiting Mg to carbonate ion (Fig. 3e), the boron concentration of the

443 solution (which might induce disproportional increase in B incorporation; Allen and

444 Hönisch, 2012) (Fig. 3f), the ionic strength of the solution (which might enhance B

445 incorporation; e.g. Kitano et al., 1978) (Fig. 3g), or $([Ca^{2+}]*[CO_3^{2-}])/([Ca^{2+}]+[CO_3^{2-}])$, found to be

446 a useful predictor of ACC precipitation rate by Evans et al. (2020) (Fig. 3h). Finally, there is no

447 correlation between residual B/Ca variability and the degree to which these carbonate

448 samples diverged from oxygen isotope equilibrium (Supp. Fig. 11), which again suggests

449 kinetics are not the dominant factor dictating B incorporation in our experiments.
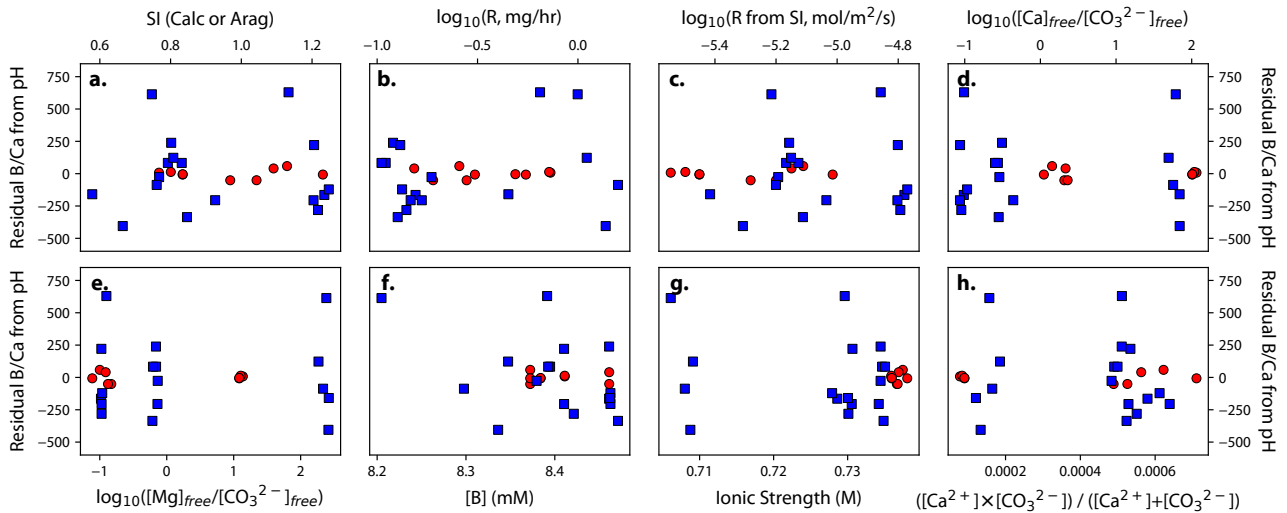
Figure 3: *Residual variability from the B/Ca-pH relationship observed in Fig. 2a against experimental solution and measurement parameters. As in Fig. 2, calcites are shown as red circles, and aragonites as blue squares. No correlations are observed between a) solution Saturation Index (note aragonites plotted against SI_{arag}, calcites vs. SI_{calc}), b) precipitation rate parameterized as mass of carbonate grown per hour, c) precipitation rate based on the relationship between SI and R following Farmer et al. (2019), d) Calcium to carbonate ion ratio, e) Mg concentrations relative to carbonate ion, f) total boron concentration in solution, g) ionic strength or h) CaCO_3 product over sum.*

Despite there being little correlation between residual B/Ca and experimental parameters, there is a strong correlation, consistent across both polymorphs ($R^2_{Calc} = 0.74$; $R^2_{Arag} = 0.64$), between B/Ca and Na/Ca (Fig. 4a), which in the case of aragonite is much stronger than the relationship between either element and any carbonate system or saturation parameter. This apparent importance of Na/Ca is also evident in strong correlations between residual B/Ca variability around the pH trend and Na/Ca, particularly in aragonite (Fig. 4b). When such a consistent B/Ca-Na/Ca relationship is observed across both polymorphs, without an evident causal driver among solution chemistry parameters, one might infer some artefact of analysis or sample preparation. However, our sample cleaning protocol was consistent across all samples, and variability does not correspond to different analytical or sample preparation batches. Furthermore, there is little support for inaccuracy of matrix matching between sample and standard during ICPMS analysis (which may bias measurements of B/Ca; Yu et al., 2005) introducing significant residual variability in B/Ca (Supp. Fig. 12).
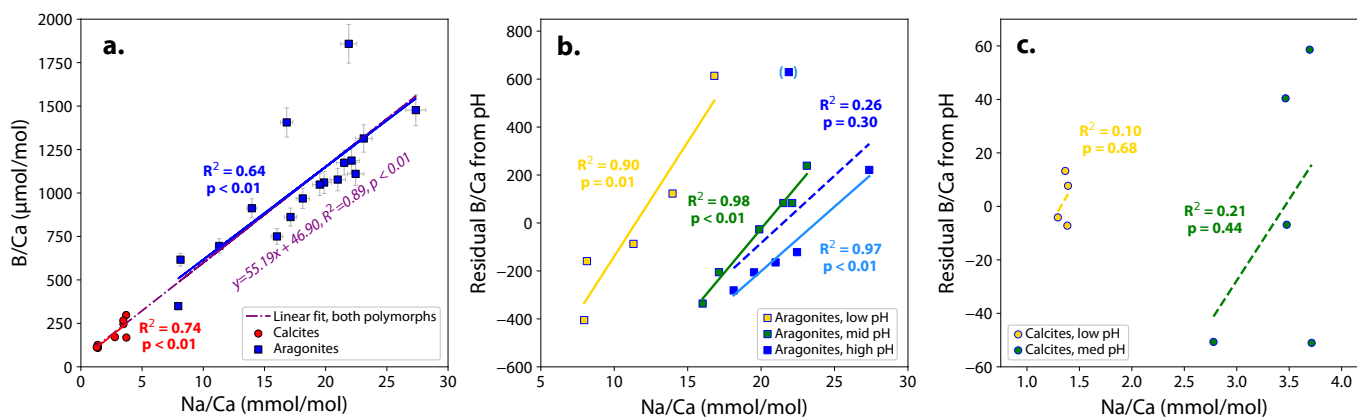
Figure 4: a) Measured B/Ca vs. Na/Ca ratios in calcites (red circles) and aragonites (blue squares). R-squared values for calcites, aragonites and both polymorphs together are higher than, or comparable to, correlations with any aqueous chemical parameters. Additionally, slopes of linear regressions plotted through either dataset (red and blue lines) are indistinguishable and can be equally well fit with a relationship through both polymorphs (purple line, equation inset). To visualise this another way, in aragonites, as shown in panel b, residual B/Ca around the pH relationship shown in Fig. 2 is strongly correlated with Na/Ca ratios for low and medium pH experiments. At higher pH, an outlier (marked in lighter blue brackets) means that this relationship is not significant (dashed blue line), but when this outlier is removed the relationship between residual B/Ca and Na/Ca is strong for all other datapoints (light blue). For calcites (panel c), the magnitude of residual B/Ca and Na/Ca variability is much lower, and no statistically significant relationships are observed, although regression lines through both low and medium pH calcites are strongly positive, as in aragonites.

3.3 Boron isotopes

Boron isotope compositions of experimental solutions and precipitates are given in Table 2. We observed no difference outside of analytical uncertainty in solution $\delta^{11}B$ between experiments, and no systematic drift in $\delta^{11}B$ within individual experiments (Table 2). Therefore, for calculating aqueous $\delta^{11}B_{borate}$ and interpreting our data we assume a value of -14.34 ± 0.03 ‰ (2se), which is the mean and two standard errors of our solution measurements (n = 31). Measured carbonate $\delta^{11}B$ values range from -18.85 to -38.53 ‰. To aid comparison of our experimental data with other experimental data and data from natural carbonates, we normalise all carbonate data to a natural seawater $\delta^{11}B$ of 39.61 ± 0.04 ‰ (Foster et al., 2010), using the approach for dealing with modified seawater outlined by Zeebe and Wolf-Gladrow (2001). Since [Mg] and [Ca] (and hence pK^*_B) varied between our experiments, and between published experiments, $\delta^{11}B_{CaCO3}$ is plotted as a function of $\delta^{11}B_{borate}$ in Fig. 5 rather than pH, alongside our new measurements of Sanyal et al. (2000)'s

500 precipitates, existing published data from Noireaux et al. (2015), Kaczmarek et al. (2016a)

501 and Farmer et al. (2019). Our new measurements of Sanyal et al. (2000)'s carbonates are

502 broadly similar to the original NTIMS data at high pH, but diverge at low pH, giving a pH

503 sensitivity (i.e. a slope) that is much closer to aqueous borate than previous data suggested

504 (0.99 vs. 0.83; Fig. 5 and Supplementary Appendix), with the aforementioned caveat that we

505 cannot confirm the efficacy of our rinses. For our own carbonates, as documented by

506 Noireaux et al. (2015) over a more limited range in solution pH, we observe that $\delta^{11}B_{aragonite}$

507 closely follows that of $\delta^{11}B_{borate}$, but that $\delta^{11}B_{calcite}$ diverges progressively from $\delta^{11}B_{borate}$ as pH

508 decreases, with a slope (i.e. a pH sensitivity) of considerably less than unity (m=~0.5). That

509 said, our calcite data sit closer to the $\delta^{11}B_{borate}$ line than other previous inorganic calcite

510 precipitates (Fig. 5). Also similar to Noireaux et al. (2015), we observe a slope that is slightly

511 less than 1 for the fit between $\delta^{11}B_{aragonite}$ vs. $\delta^{11}B_{borate}$ calculated from an equilibrium

512 fractionation factor between boric acid and borate (α_B, sometimes denoted $^{11\text{-}10}K_B$) of 1.0272

513 (Klochko et al., 2006; see Fig. 5a), and a slightly better fit with the 1:1 line for an α_B of 1.026

514 (Nir et al., 2015; see Fig. 5b). Indeed, to quantitatively determine the best fit of α_B to the

515 combined body of aragonite data from Noireaux et al. (2015) and our aragonite data

516 (accounting for uncertainty in each datapoint), we used SciPy.optimization (SciPy 1.0

517 Contributors et al., 2020), and derive an α_B of 1.02607: strikingly similar to that proposed

518 independently by Nir et al. (2015).

519
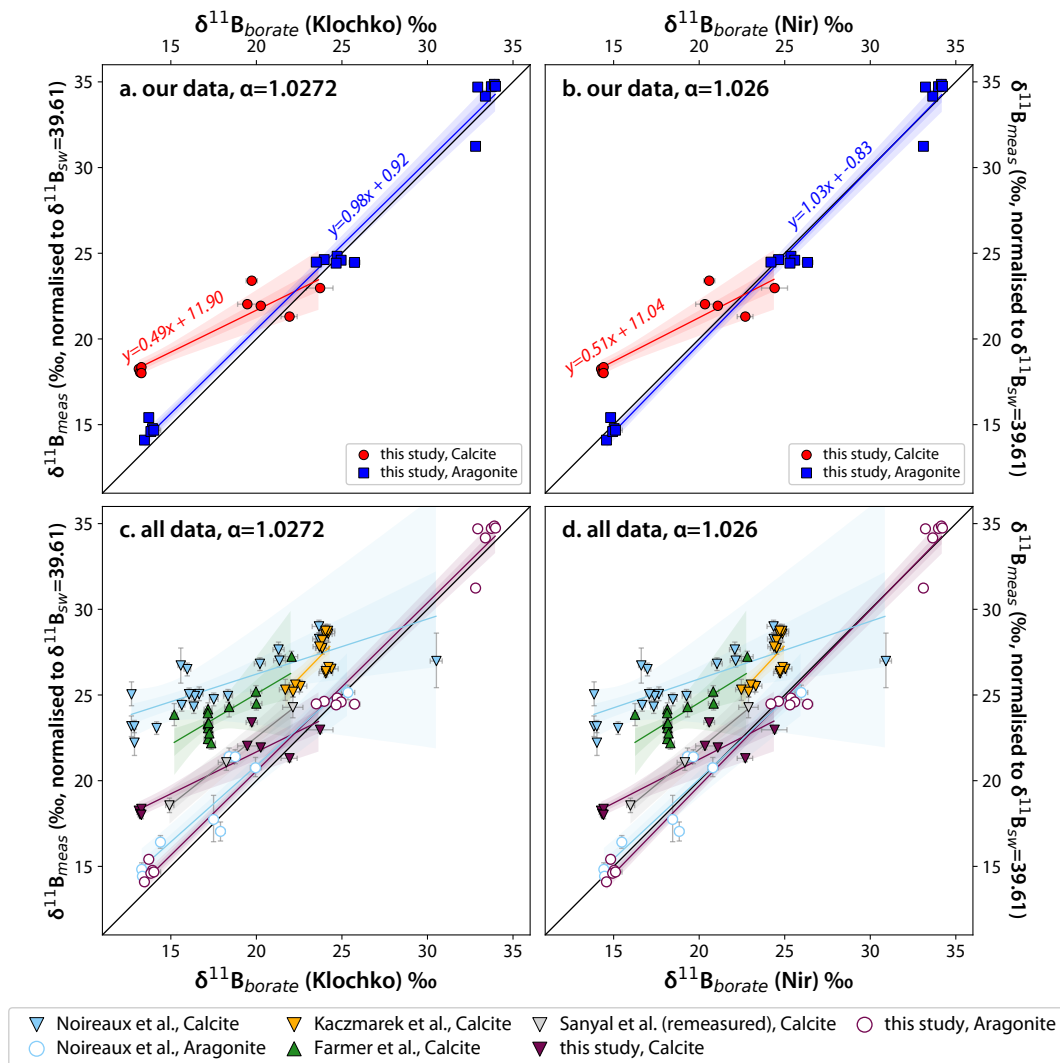
Figure 5: Boron isotope measurements in calcites (red circles) and aragonites (blue squares) from our study, normalised to a natural seawater value of 39.61 ‰ (Foster et al., 2010) and plotted against $\delta^{11}B_{borate}$ calculated according to an α_B of 1.0272 (panel a; Klochko et al., 2006) and 1.026 (panel b; Nir et al., 2015). In panels c and d, our data (in claret) are shown in the context of data from Noireaux et al. (2015; blue), Kaczmarek et al. (2016a; gold) and Farmer et al. (2019; green), as well as the remeasured calcites from Sanyal et al. (2000; grey). Calculated values plotted here use the 'pitzer.dat' database in PHREEQC (Charlton and Parkhurst, 2011b). Error bars on $\delta^{11}B_{carbonate}$ are Monte Carlo propagated 95% confidence intervals, incorporating uncertainty from measurement and uncertainty in experimental fluid $\delta^{11}B$ during the experiment. Error bars on $\delta^{11}B_{borate}$ are Monte Carlo propagated 95% confidence intervals, incorporating uncertainty from drift in pH and experimental fluid chemistry (and hence pK^*_B) during the experiment. Regression lines plotted, and their 1 and 2 σ confidence intervals (lightly and darkly shaded regions respectively), are constructed using a Monte Carlo 'wild bootstrap' approach (Liu, 1988; Mammen, 1993), where predictor variables are fixed and the regression t-statistic is resampled instead, an approach which is better suited to small datasets (Cameron et al., 2008; Imbens and Kolesar, 2012).

4 Discussion

4.1 Elemental partitioning: Na and Mg

The reduction in Na partitioning into both calcite and aragonite we observe with increasing pH (Fig. 2) is counter to the observations of Busenberg and Plummer (1985), who precipitated synthetic calcites from Na-Ca-S-K-Cl solutions with the stated aim of investigating the link between growth rate and Na incorporation. Their study revealed a similarly positive correlation between Na incorporation and pH, but in their study Na partitioning (D_{Na}) also increased with pH or SI. We also see a positive trend in D_{Na} with pH, albeit to a lesser extent, in the remeasured calcites of Sanyal et al. (2000) (Supp. Fig. 13). Busenberg and Plummer (1985) concluded that the incorporation of Na a) followed a Freundlich isotherm (indicative of adsorption behaviour, rather than straightforward Nernst partitioning), b) increased with growth rate ($R^2 = 0.25$, $p = 0.04$), c) was linked to the number of defect sites in the calcite structure, and d) itself increases the lattice spacing of the calcite. These latter two observations are supported by subsequent research which reproduced a rate effect on Na partitioning (Mucci, 1988) and demonstrated that Na is hosted in substitutional defect sites, not interstitial sites (Yoshimura et al., 2017). The decrease in D_{Na} we observe with pH and SI could therefore simply be a result of lower bulk precipitation rates (in mg/hr) in our higher pH/SI calcite and aragonite experiments (Supp. Fig. 4), in contrast to a strongly positive correlation ($R^2 = 0.79$, $p < 0.01$) between pH and precipitation rate in Busenberg and Plummer's experiments. However, if this implies that our bulk precipitation rate estimates are indeed an accurate proxy for crystal-surface-scale precipitation rate, this has implications for our boron incorporation/isotope data (discussed later). Additionally, we note that Füger et al. (2019) observed a similar negative trend in Na partitioning with pH, which they attributed not to changing precipitation rate, but a lower prevalence of HCO_3^- ion to be incorporated into the $CaCO_3$ lattice to balance the incorporation of monovalent Na^+. This effect would not be apparent in the experiments of

566   Busenberg and Plummer (1985), because their experimental pH never reached values high

567   enough for carbonate speciation to begin to move from HCO_3^- to CO_3^{2-}. It is unlikely, then,

568   that Na partitioning is a straightforward reflection of precipitation rate alone.

569   In the case of Mg, we see little change in partitioning in calcite with pH or SI, but we

570   observe higher D_{Mg} with higher pH/more saturated conditions in aragonites (Figs. 2h,j).

571   However, in light of inconsistent responses of Mg partitioning to precipitation rate in

572   published aragonite precipitation experiments (Gabitov et al., 2008; Mavromatis et al., 2013),

573   it is similarly difficult to infer anything about precipitation rate in our experiments from this

574   finding.

4.2 Elemental Partitioning: B

576   We observe a strong carbonate system control on B incorporation into both calcites

577   and aragonites, concordant with the fundamentals of the boron isotope and B/Ca palaeo-

578   proxies, although there is considerable B/Ca variability evident around these relationships

579   (Fig. 3). While we explore any potential aqueous chemical conditions that could have

580   secondarily influenced carbonate B incorporation (Fig. 3), given that within each pH

581   treatment there was relatively little variability in solution chemistry but considerable

582   variability in B/Ca (and Na/Ca), it follows that no obvious correlations arise. Instead, B

583   incorporation exhibits apparently stochastic variability around a predominant carbonate

584   system control within our dataset, variability which is particularly evident in aragonites. This

585   variability, without apparent correlation with any of our (albeit perhaps imperfect)

586   measured growth rate indicators (Fig. 3), would not be expected if incorporation rigidly

587   follows the surface kinetic model of Branson (2018) with a set rate of attachment and

588   detachment for both aqueous boron species at any given mineralogy and solution

589   chemistry. Indeed, in our dataset, the highest bulk precipitation rates correspond to lower

590   λ_B values (Supp. Fig. 14). It may well be that our experimental carbonates were more highly

591   influenced by the same secondary control on B incorporation that drives the residual

592   unexplained variability in λ_B observed by Farmer et al. (2019), which these authors suggested

593   may be linked to some other control on binding site availability.

594   One such control on binding site availability, indicated by the close correlation we

595   observed across both calcites and aragonites between Na enrichment and B enrichment

596   (Fig. 4a), and the coherence between residual B/Ca variability and Na/Ca (Figs. 4 b, c) is the

597   provision of B incorporation sites via Na substitution. Na^+ substitutes for Ca^{2+} in calcium

598   carbonate rather than being incorporated at interstitial sites (Yoshimura et al., 2017), and

599   thus a means to maintain charge balance in the crystal lattice is required. Paired

600   incorporation of Na^+ and $B(OH)_4^-$ in place of Ca^{2+} and CO_3^{2-} may be one such mechanism.

601   Indeed, the consistency of this relationship across both carbonate polymorphs, with an

602   intercept close to the origin, suggests that paired incorporation of Na and B may be the

603   primary means by which B can be incorporated into $CaCO_3$ lattice (note, given the order of

604   magnitude greater concentration of Na in $CaCO_3$, it is unlikely to be the other way around).

605   This could also be the basis by which salinity or [Na] enhances B incorporation in inorganic

606   carbonates (Kitano et al., 1978; Uchikawa et al., 2017) and perhaps even biogenic carbonates

607   (Allen et al., 2012). Moreover, if the incorporation of Na into defect sites distorts the $CaCO_3$

608   lattice structure as it grows (Busenberg and Plummer, 1985), it may follow that Na

609   incorporation is multiplicative, with a more disordered lattice potentially enhancing further

610   substitution of Na^+ for Ca^{2+}, and more $B(OH)_4^-$ with it. In this way, the apparent stochasticity

611   of our B/Ca data in relation to solution chemistry, but their systematic correlation with

612   precipitate Na/Ca, could be explained by differences in the frequency and timing of Na

613   substitution during the nucleation or early growth of experimentally-grown $CaCO_3$,

614   potentially setting the regime for B incorporation thereafter.

615

616   **4.3 Boron isotope incorporation: aragonite vs calcite**

617   In common with previous studies, we observe relatively poor agreement between

618   the $\delta^{11}B$ of our synthetic calcite and aqueous $\delta^{11}B_{borate}$, considerable scatter between

619   experimental treatments, and a slope (i.e., a pH sensitivity) that is much less than 1 (Fig. 5).

620   In the case of aragonite, however, we observe that $\delta^{11}B_{aragonite}$ closely resembles that of

621   aqueous $\delta^{11}B_{borate}$, confirming the findings of Noireaux et al. (2015) over a wider pH range

622   (~7.4 – ~9.4). That the relationship between $\delta^{11}B_{aragonite}$ and aqueous $\delta^{11}B_{borate}$ observed here

623   is within uncertainty of that observed by Noireaux et al. (2015) is also significant in itself,

624   since the solution chemistries, ionic strengths, and precipitation techniques used differ

625   considerably between our study and this previous work. For instance, the ionic strength of

626   our solutions was close to mean average seawater ($I = 0.7$ M), whereas it was considerably

627   lower ($I = 0.1$-0.2 M) in the experiments of Noireaux et al,. (2015). Therefore, we can conclude

628   that at least in aragonites, solution chemistry appears to have little intrinsic influence on the

629   isotopic partitioning of boron beyond its calculable effect on boron speciation, and that sole

630   incorporation of borate ion, without fractionation during any adsorption step, is strongly

631   implied. With regards the value of α_B, our analyses suggest that an α_B of 1.026 (from Nir et

632   al., 2015) produces a better fit with $\delta^{11}B_{aragonite}$ compared to the α_B of 1.0272 from Klochko et

633   al. (2006). At this stage, we cannot discern whether this supports this later estimate of the

634   fractionation factor between aqueous borate and boric acid as being more accurate (as

635   argued by Noireaux et al. 2015), or whether this is some aragonite-specific fractionation

636   from aqueous borate. In practical terms for the application of the boron isotope-pH proxy,

637   in instances where empirical calibrations are used this should not matter greatly, provided

638   the same value of α_B is used in calibration and reconstruction. However, in cases where a

639   pH-sensitivity equal to aqueous borate is assumed, this should be borne in mind-

640   particularly in the reconstruction of calcification fluid pH from aragonitic coral $\delta^{11}B_{aragonite}$

641   (e.g. Holcomb et al., 2014; Schoepf et al., 2017).

642   While the boron isotope composition of our calcite precipitates, as with previous

643   studies, diverges significantly from that calculated for aqueous borate ion, it is notable that

644   our precipitates fall closer to $\delta^{11}B_{borate}$ than other previously published carbonate data (Fig.

645   5). Indeed, at the upper end of the pH range of our calcite experiments (~8.6), our calcite

646   precipitates record the $\delta^{11}B_{borate}$ more or less faithfully, which speaks against the existence

647   of a universal boron isotope fractionation during adsorption and incorporation at this pH

648   that has been observed elsewhere (Saldi et al., 2018). Possible mechanistic reasons for this

649   are discussed further in the next section, but we suggest that the higher ionic strength of

650   our precipitation solutions may be key. Saldi et al. (2018) observed that the apparent

651   magnitude of fractionation associated with adsorption onto calcite decreased with

652   increasing ionic strength (*I*), although we note their estimates of the fractionation were also

653   more uncertain with increasing *I*. We note that proximity in measured $\delta^{11}B$ to aqueous

654    $\delta^{11}B_{borate}$ increases with ionic strength, with our data and those remeasured calcites of Sanyal

655   et al. (2000) – both precipitated at *I* = ~0.7 mol/kg – closest in measured $\delta^{11}B$ to aqueous

656   borate ion, and Kaczmarek et al. (2016b)'s calcite precipitations (*I* = ~0.6 mol/kg), next

657   closest. Therefore we suggest that isotope fractionation upon adsorption of B onto calcite,

658   while evidently large at low ionic strength (Saldi et al., 2018), is much weaker (and possibly

659   negligible) at ionic strengths typical of seawater conditions. Our data also appear

660   incompatible with the large structural fractionation between aqueous and solid carbonate-

661   hosted B phase advocated by Balan et al. (2016; 2018), perhaps supporting Farmer et al.

662   (2019)'s assessment that simulations at close to thermodynamic equilibrium are likely

663   unrepresentative of conditions at a growing mineral face.

664   Although the remeasured precipitates of Sanyal et al. (2000), if reliable, show a slope

665   that is much more similar to aqueous borate than when measured via NTIMS (Fig. 5,

666   Supplementary Appendix), and our calcite data in general fall closer to the $\delta^{11}B$ of aqueous

667   borate ion than previous studies, our calcites nonetheless diverge strongly from $\delta^{11}B_{borate}$ at

668   low ambient $\delta^{11}B_{borate}$ (/pH), with a slope considerably less than unity (~0.49-0.51) and

669   considerable scatter (Fig. 5). The offset between measured $\delta^{11}B_{carbonate}$ and aqueous $\delta^{11}B_{borate}$

670   Δ_{C-B} (note we use Δ here rather than ε to avoid confusion with the aqueous fractionation

671   between borate and boric acid, ε_B) in our calcites falls roughly upon the same relationship

672   with SI described by other published data (and as noted by Farmer et al., 2019). Specifically,

673   Δ_{C-B} values approach $\delta^{11}B_{borate}$ at high SI, and are increasingly positively offset at low SI (Fig.

674   6a). According to the SKM model of Branson (2018), the mechanism for this trend is that

675   rates of precipitation are faster than those of detachment of $B(OH)_4^-$ ion from the crystal face

676   at higher SI. Conversely, precipitation rates are lower at low SI, and relatively higher

677   detachment of $B(OH)_4^-$ leaves the bulk crystal relatively enriched in trigonal $B(OH)_3$, whose

678   detachment rates are lower. However, as previously discussed, unlike the data of Farmer et

679   al. (2019), SI was if anything negatively correlated with measured bulk precipitation rate in

680   our calcite experiments (see Supp. Fig. 4), and higher bulk precipitation rates in lower pH

681   treatments correspond to the most elevated $\delta^{11}B_{carbonate}$ relative to aqueous $\delta^{11}B_{borate}$.

682   Moreover, if high precipitation rate were the key in trapping $B(OH)_4^-$, one might expect those

683   samples that precipitated furthest from oxygen isotope equilibrium to have the smallest

684   values of Δ_{C-B}, but if anything those closest to Kim & O'Neil (1997)'s estimate of equilibrium

685   fractionation most closely resemble aqueous $\delta^{11}B_{borate}$ (Fig. 6b). Finally, there are reasons

686   within the dataset of Noireaux et al. (2015) to suspect that rate may not be the primary factor

687   at play: a) the only calcite precipitate from above pH 9 is inconsistent with such a model and

688   b) seeded and unseeded calcites in their experiments showed different surface-area-

689   normalised precipitation rates, and yet this is not reflected in their Δ_{C-B}.
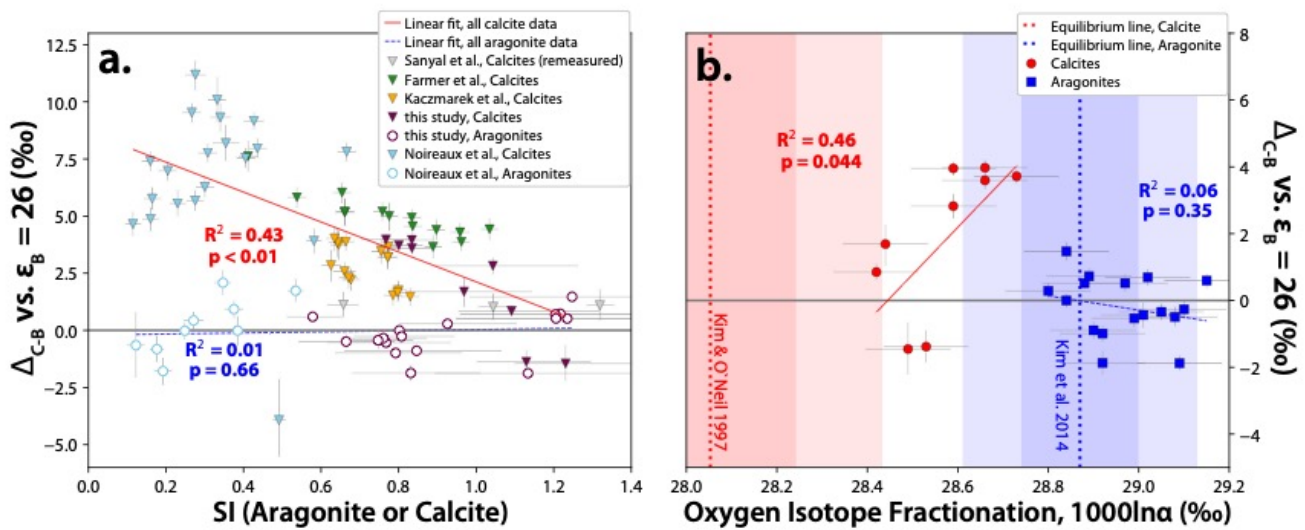
Figure 6: The offset Δ_{C-B} between $\delta^{11}B$ measured in calcite precipitates and the predicted $\delta^{11}B$ of aqueous borate in their experimental growth media (assuming $\varepsilon_B = 26$ ‰, from Nir et al. (2015)) correlates with SI ($R^2 = 0.43$; panel a), which is a common driver of precipitation rate. However, there is considerable scatter in the calcite data from Noireaux et al. (2015) that do not fit this relationship. It may therefore be incorrect to treat SI as a universal proxy for precipitation rate, since in our experiments SI does not correlate well with bulk precipitation rate (Supp. Fig. 4). Furthermore, one might expect the fastest rates of precipitation at high SI, and yet in our study the largest deviations from oxygen isotope equilibrium (panel b), which in the case of calcites also showed the greatest offset from the $\delta^{11}B$ of aqueous borate, were at the lowest SI values. This is inconsistent with increasing $B(OH)_4^-$ incorporation relative to $B(OH)_3$ at high precipitation rates, advocated by Farmer et al. (2019). Data in panel b are plotted in relation to the calcite equilibrium oxygen isotope fractionation of Kim & O'Neil (1997) (red dotted line) and the aragonite equilibrium oxygen isotope fractionation of Kim et al. (2014) (blue dotted line).

4.4 Possible reconciliation of disparate findings with surface zeta potential

Although we demonstrate that boron incorporation into aragonite adheres to the established basis of the boron isotope proxy across a wide range of pH, the variability in boron partitioning and isotope fractionation within our calcite data and between published calcite datasets continues to pose a challenge to this paradigm. We suggest, however, that some of this variability might be explicable when one considers the surface coordination environment of the contact solution. For B, Na and Mg to be incorporated into the $CaCO_3$ lattice structure, these ions must first adsorb onto electrostatically-favourable mineral surface sites. The possible exception to this is Mg in aragonite, where adsorption behaviour is not always evident (De Groot and Duyvis, 1966; Mucci and Morse, 1983). Both Na (e.g. Busenberg and Plummer, 1985) and B (Goldberg and Forster, 1991; Saldi et al., 2018; Wang

715 et al., 2018) follow Langmuir adsorption isotherms, suggesting adsorption is the critical first

716 step on the pathway to their incorporation. Typically, sorption reactions are discussed in

717 relation to a mineral's surface charge. In the case of most metal oxides surface charge is

718 determined by the relative concentrations of H^+ and OH^- ions (the 'potential determining

719 ions', or PDIs) in solution (e.g. Schindler and Stumm, 1987), and thus it is pH dependent.

720 However, surface electrostatic behaviour of $CaCO_3$ is more complex, as free Ca^{2+} and CO_3^{2-}

721 ions (whose speciation itself may be pH dependent) are instead the principle PDIs (Foxall et

722 al., 1979). Indeed, as summarised by Al Mahrouqi et al. (2017), varying pH while keeping pCa

723 constant will not change the electrostatic behaviour of calcite. This, coupled with the

724 solubility of $CaCO_3$ in water and the fact that one of the PDIs, CO_3^{2-}, is also sensitive to

725 equilibration with the atmosphere, has meant that published measurements of $CaCO_3$

726 surface potential have often been inconsistent (see Wolthers et al., 2008; Al Mahrouqi et al.,

727 2017 for a summary).

728 Additionally, unlike in the case of metal oxides, the effective surface charge of $CaCO_3$

729 in water is not in itself sensitive to pH: a well-ordered water layer exists at the interface of

730 the mineral (Fenter et al., 2000; Fenter and Sturchio, 2004; Geissbühler et al., 2004), termed

731 the hydrolysis layer (Stipp, 1999) or 0-plane (Heberling et al., 2011), and at this plane the

732 charge should be weakly negative across a wide range of pH (5.5-11; Heberling et al., 2011).

733 The parameter that controls an affinity of the carbonate surface for dissolved anions or

734 cations in the bulk solution is therefore not the surface charge of the terminal edge of the

735 mineral lattice, as is often discussed (e.g. Branson, 2018; Saldi et al., 2018), but the zeta

736 potential (ζ-potential), which is defined as the electrostatic potential at the outer Helmholtz

737 plane (OHP; the outermost plane of the Stern layer, where strongly bonded hydrated cations

738 reside in fixed-positions coordinated with the terminal edge, see Fig. 7 for a schematic).

739 Between the Stern layer and the bulk solution (where potential = 0 mV) lies the diffuse layer,

740 where anions and cations are mobile, and will be repelled or attracted to the OHP according

741 to their charge. Together, the hydrolysis layer, Stern layer (including inner and outer

742 Helmholtz planes) and diffuse layer make up the 'electric double layer' or EDL (see helpful

743 summaries in Stipp, 1999; Al Mahrouqi et al., 2017). When viewed within this framework, the

744 steps which an ion must go through to be incorporated in the solid phase are: a) migration

745 through the potential gradient in the diffuse layer, b) adsorption at, and lateral migration

746 along, the Stern layer, and c) removal of the chemi-sorbed OH^- and H^+ at the termination of

747 the mineral lattice in the hydrolysis plane such that the ion can finally meet its binding site

748 and coprecipitate. Solution chemistry will likely have effects on all of these steps, but we

749 particularly focus on the first two here.
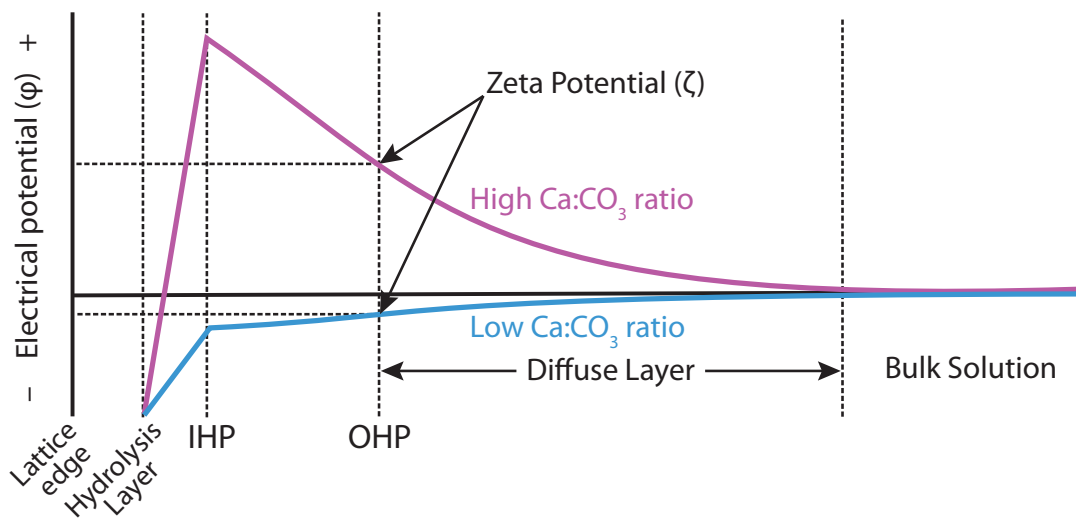
750 *Figure 7: Schematic representation of electrostatics at the mineral face, from the first hydrolysis*
751 *layer (Heberling et al., 2011), through the inner Helmholtz plane (IHP; where ions are specifically*
752 *adsorbed to the mineral face), outer Helmholtz plane (OHP; where ions are non-specifically*
753 *adsorbed, retaining their hydration shell), and diffuse layer, where ions are electrostatically*
754 *attracted to or repulsed by the charge at the OHP (i.e. the zeta potential), but can move around.*
755 *The ratio of potential-determining ions (PDIs) Ca^{2+} and CO_3^{2-} will alter the zeta potential.*
756
757 Considering the observed ζ-potential of a growing carbonate mineral, which is weakly

758 negative in most natural settings (e.g. Berlin and Khabakov, 1961; Cicerone et al., 1992; Al

759 Mahrouqi et al., 2017), rather than charge at the terminal layer of the crystal, which is

760 typically considered to be positive (e.g. Kitano et al., 1978; Branson, 2018), the attraction and

761 adsorption of only tetrahedrally co-ordinated B (i.e. $B(OH)_4^-$) to carbonate minerals becomes

762 more difficult to explain. One potential route for $B(OH)_4^-$ (and not $B(OH)_3$; Saldi et al. (2018))

763   to migrate against a gradient in electrostatic potential and adsorb at the Stern layer could

764   be attraction as part of a complex with aqueous Ca^{2+} ($CaB(OH)_4^+$) or Mg^{2+} ($MgB(OH)_4^+$). These

765   complexes can host up to 19 % of the dissolved tetrahedral $B(OH)_4^-$ within the experimental

766   solutions examined here, as calculated using the pitzer.dat database, suggesting this is not

767   unreasonable. Such a mechanism might also help to explain the decrease in $B(OH)_4^-$

768   adsorption to the calcite surface at high pH (Saldi et al., 2018), despite ζ-potential likely

769   remaining similarly negative at higher pH, since at high pH much less $B(OH)_4^-$ ion is

770   complexed with Ca^{2+} or Mg^{2+} in relative terms. Uncharged $NaB(OH)_4$ ion pairs might also

771   provide a vector for $B(OH)_4^-$ to cross this electrostatic gradient, with this ion pair either then

772   being incorporated together by paired substitution or dissociated at the Stern layer.

773   In the absence of other influences, the concentrations of the main PDIs (Ca^{2+} and CO_3^{2-}

774   ) in a solution will affect the magnitude (and perhaps sign) of the ζ-potential, by altering the

775   coverage density of PDIs at the Stern layer. At higher concentrations of Ca^{2+}, i.e. lower pCa,

776   ζ-potential in carbonates gets progressively more positive (Al Mahrouqi et al., 2017), thereby

777   reducing the potential energy needed to bring a negatively-charged ion to the OHP. Other

778   ions in solution may also act as PDIs. Although Ca^{2+} and CO_3^{2-} are the primary PDIs, Mg^{2+} is

779   thought to also affect calcite ζ-potential almost, or just as strongly as Ca^{2+} (Cicerone et al.,

780   1992; Al Mahrouqi et al., 2017), and even Na^+, often considered an indifferent ion, may act

781   as a PDI in some settings (Al Mahrouqi et al., 2017). Others have observed that PO_4^{3-} in

782   solution, which has been shown to influence B incorporation (Henehan et al., 2015;

783   Uchikawa et al., 2017), also lowers calcite ζ-potential (Douglas and Walker, 1950;

784   Amankonah and Somasundaran, 1985). In the case of published boron-carbonate

785   coprecipitations, most studies (ours included) have attempted to maintain roughly constant

786   saturation (and hence precipitation rate) at low pH by compensating for the lack of aqueous

787   CO_3^{2-} ion with increases in [Ca^{2+}]. Although this keeps Ω roughly constant, by altering the

788   ratio of these important PDIs, the resultant changes in ζ-potential (and hence the ease at

789   which positive vs. negative ions reach the OHP surface) are likely much larger than would

790   ever be seen in natural systems. With this in mind, plotting the residuals from the

791   relationship between experimental calcite Δ_{C-B} and SI (Fig. 8a) against the ratio of the key

792   PDIs in solution yields a strong correlation (Fig. 8b), suggesting that the ratio of PDIs plays a

793   parallel role in influencing boron incorporation, and may well be the unknown secondary

794   control hinted at by Farmer et al. (2019). Together, SI and the ratio of PDIs can explain 73%

795   of the variability in Δ_{C-B} seen in experimental calcites to date (Fig. 8c), although we note that

796   factors other than the ratio of these two PDIs can influence ζ-potential, and as such it may

797   be that electrostatics play a role in explaining the other 27 % of observed variance.

798   Promisingly, the PDI ratio can explain much of the variability in the calcites of Noireaux et al.

799   (2015) that are otherwise poorly explained (Fig. 6) by an SI or precipitation rate-driven

800   scenario (Farmer et al., 2019), without needing to discount any data points as outliers. That

801   these data should be the most influenced by PDI ratio is consistent with expectations from

802   the electric double layer, because ionic strength in solution determines the thickness of the

803   diffuse layer (essentially because at higher ionic strengths there are more charged ions

804   contained within the diffuse layer with which charge can be balanced). Generally speaking,

805   this means that at higher ionic strengths, the ζ-potential of $CaCO_3$ is closer to zero, and is

806   less easily perturbed by other experimental parameters (e.g. Glover et al., 2012; Al Mahrouqi

807   et al., 2016). Thus, the effect of changes in experimental conditions on ζ-potential are likely

808   to be much greater for lower ionic strength experiments such as Noireaux et al. (2015)'s ($I =$

809   0.1 - 0.2 M), than for conditions closer to seawater. This phenomenon is further evidenced

810   in the experiments of Saldi et al. (2018), where the amplitude of change in boron adsorption

811   with carbonate system change was progressively dampened with higher ionic strength -

812   consistent with a collapsing of the diffuse layer.

813   One other experimental parameter that may influence the ζ-potential of $CaCO_3$ is the

814   amount of mineral surface relative to experimental solution, with observed ζ-potential

815   varying with specific surface area (e.g. Vdović, 2001). As boron and other impurities will

816   produce more surface roughness on a growing crystal face (Dove et al., 2004; Ruiz-Agudo et

817   al., 2012), as well as altering its surface charge (notwithstanding possible compensation in

818   the hydrolysis plane), it is therefore conceivable that positive feedbacks might emerge

819   between incorporation of impurities and changing ζ-potential, thus accentuating stochastic

820   variation in element partitioning, and perhaps isotope fractionation. Relatedly, the

821   concentration of solid grains in an experimental solution – which varies considerably

822   between and within the experiments examined here – may also affect ζ-potential, with

823   increasing solid-liquid ratios making ζ-potential more positive (Siffert and Fimbel, 1984;

824   Vdović, 2001; Wang et al., 2018), and more so in calcites than aragonites (Wang et al., 2018),

825   although it is unclear if all such observations are at equilibrium pCa (Al Mahrouqi et al., 2017).

826   While we see no correlation between particle density (in mg/L) and residual variability

827   around our multivariate model, we highlight this issue for consideration when designing

828   future precipitation experiments.

829   Considerations of ζ-potential may also help to explain the differences observed to

830   date in boron co-precipitation behaviour between natural and synthetic calcites. Synthetic

831   calcites show consistently more variable ζ-potential than natural or biogenic calcites (Al

832   Mahrouqi et al., 2017, and references within), and may be positive or negative. Biogenic

833   calcites, however, display (with few documented exceptions) weakly negative ζ-potential,

834   *Figure 8: Δ_{C-B} – the offset between measured $\delta^{11}B$ in calcite precipitates and predicted $\delta^{11}B$ of*
835   *aqueous borate (calculated at $\varepsilon_{B_r} = 26$ ‰) – correlates reasonably well with SI, as seen in other*
836   *studies (panel a), although there is significant unexplained variability – particularly visible in the*
837   *data of Noireaux et al. (2015). Plotting the residuals from this relationship the ratio of PDIs in*
838   *solutions, however, can explain the majority of this residual variability (panel b)- suggesting that*
839   *variable ζ-potential in experimental setups may play a role in explaining observed patterns. With*
840   *these two variables alone, 73% of the variance in Δ_{C-B} can be explained (panel c). See electronic*
841   *supplement for animated version of panel c.*
842

843
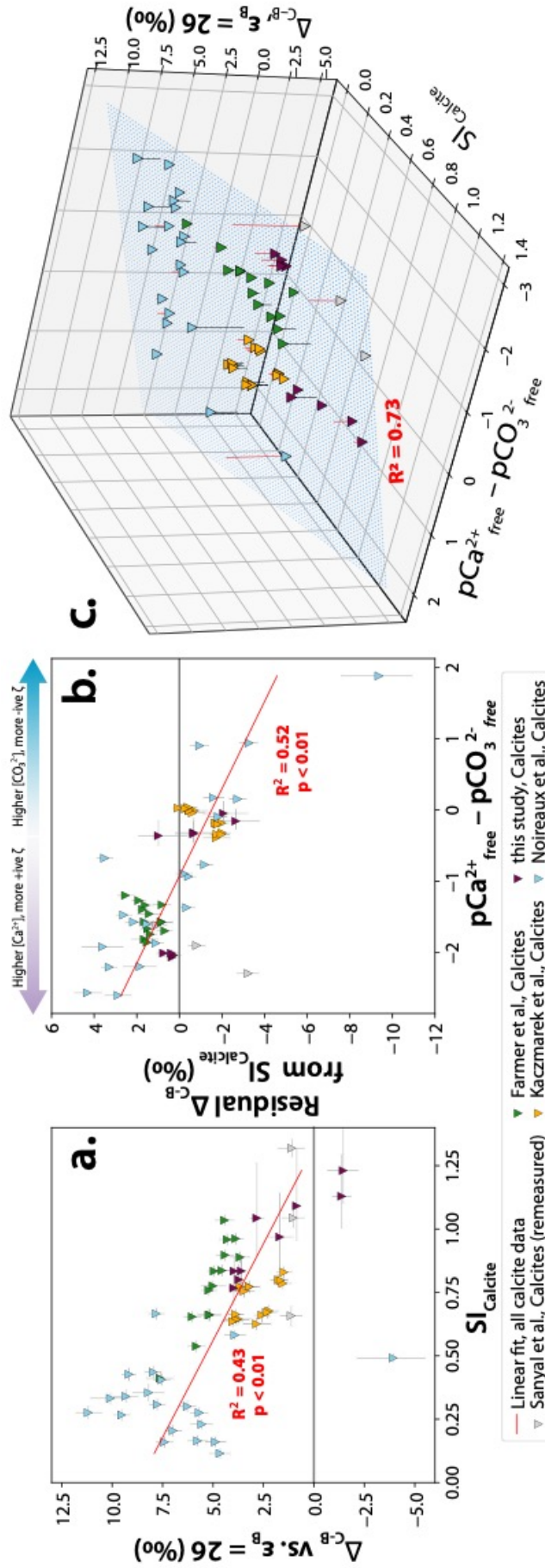
844 probably as a result of the presence of organic components (Cicerone et al., 1992; Vdović,

845 2001). This more controlled, consistently negative ζ-potential might help to explain less

846 variable boron partitioning and isotope fractionation observed in biogenic calcite (at least

847 within a species) as compared to the considerable scatter seen in synthetic calcites.

848 While patterns in our and others' inorganic precipitate measurements suggest

849 electrostatic controls on B adsorption could be a promising avenue of future research, since

850 our experiments were not designed with this in mind, we cannot put forward a more

851 complete framework for how this would induce the observed variability in $\delta^{11}B$ in synthetic

852 carbonates at this stage. However, we propose two possible models that may merit future

853 examination. Firstly, Saldi et al. (2018) note that strong electrostatic effects within the EDL

854 could alter the equilibrium isotopic fractionation of aqueous boron through the Stark effect

855 (Lambert, 1996), modifying the vibrational frequencies of the adsorbed borate relative to

856 the free borate ion. Via this scenario, stronger and more variable polarity ζ-potential in low

857 ionic strength solutions could explain the larger and more variable values of Δ_{C-B} seen by

858 Noireaux et al. (2015) compared to other studies, and the relatively weaker fractionation

859 upon adsorption with ionic strength observed by Saldi et al. (2018). Observed differences in

860 $\delta^{11}B$ between aragonite and calcite – with aragonite appearing to record aqueous borate

861 assuming Nir et al. (2015)'s aqueous fractionation factor of 1.026 across a range of ionic

862 strengths, but calcite diverging – could then be explained by relatively weaker electrostatic

863 forces (and correspondingly less sensitivity to ionic strength) at the face of the aragonite

864 polymorph. Although the vast majority of published investigations into ζ-potential are

865 motivated by industrial applications and thus have focussed on calcites, limited

866 comparisons within broader studies do suggest aragonites and calcites show different ζ-

867 potential responses to solution chemistry (De Groot and Duyvis, 1966; Smallwood, 1977;

868 Moulin and Roques, 2003), indicating this may be a fruitful avenue of investigation.

869 A second, alternative scenario, involves isotopic fractionation not associated with

870   adsorption or re-coordination of B, as is often considered (Balan et al., 2018; Saldi et al., 2018;

871   Farmer et al., 2019), but upon detachment of $B(OH)_4^-$ from the growing crystal surface. If the

872   ζ-potential of calcite is weakly negative under more natural distributions of PDIs, $B(OH)_4^-$ is

873   unlikely to be electrostatically attracted to the Stern layer – and hence the growing calcite

874   face – unless it crosses the gradient in potential in the diffuse layer as a positively charged

875   ion pair as $CaB(OH)_4^+$ or $MgB(OH)_4^+$. These aqueous ion pairs at equilibrium are not thought

876   to be strongly isotopically distinct from the free aqueous borate pool (Saldi et al., 2018).

877   However, it is conceivable that they may enhance the likelihood of kinetic isotope

878   fractionation if within the pool of e.g. $CaB(OH)_4^+$, $Ca^{11}B(OH)_4^+$ bonds are stronger or slower

879   to break than those of $Ca^{10}B(OH)_4^+$. If, while moving laterally through the Stern layer, a paired

880   Ca^{2+} ion successfully makes contact with the termination of the crystal lattice, charge balance

881   considerations mean its paired $B(OH)_4^-$ is an obstacle to incorporation. Thus either 1) the

882   Ca^{2+}-$B(OH)_4^-$ association must be broken, 2) the $CaB(OH)_4^+$ pair must be detached, or 3) this

883   boron is facilitated in the lattice, either by paired incorporation of a monovalent cation (e.g.

884   Na^+) to maintain local charge balance, or by propagation of defects in the lattice structure.

885   If $Ca^{11}B(OH)_4^+$ associations are harder (or slower) to break than $Ca^{10}B(OH)_4^+$, then the heavier

886    $Ca^{11}B(OH)_4^+$ pair is more likely to be retained long enough for either a compensating

887   monovalent cation to arrive or for the lattice to grow around the new defect. By this model,

888   negative ζ-potential (and potentially higher ionic strength) would mean more likelihood of

889   Na^+ being attracted to the Stern layer in sufficient quantity to remove the need for $B(OH)_4^-$

890   detachment (and hence fractionation). Conversely, at low pCa (more positive ζ-potential),

891   strong attraction for the divalent negative CO_3^{2-} may result in relative exclusion of Na^+ ions

892   close to the shear plane (and thus a greater propensity for kinetic fractionation due to

893   differential detachment rates) and perhaps a faster rate of entrapment at the lattice front.

894   Difference in behaviour between calcite and aragonite could then be explained by either a)

895   more consistently negative ζ-potential in aragonite, or b) a lattice structure that is more

896   accommodating of one or both of Na^+ and $B(OH)_4^-$. Furthermore, precipitation rate effects

897   could also be accommodated by this model, with faster crystal growth rates meaning a

898   greater likelihood that adsorbed $B(OH)_4^-$ is incorporated before detachment can occur.

899   **5. Conclusions: Implications for study of biogenic carbonates and the boron**

900   **isotope-pH proxy**

901   In this study, we present new $\delta^{11}B$ measurements of synthetic calcites and aragonites,

902   precipitated in the presence of Mg and at approximately seawater-like ionic strength (~0.7

903   mol/kg). B incorporation in both polymorphs increases with solution pH, although with

904   considerable variability in B/Ca within similar experimental treatments, particularly in

905   aragonites. However, a tight correlation between measured B/Ca and Na/Ca, consistent

906   across both polymorphs, may indicate an important link between Na and B incorporation at

907   the crystal surface. Although we cannot rule out the possibility that none of our metrics of

908   precipitation rate (Fig. 3, Supp Fig. 3) reflect surface area-normalised growth rates at the

909   mineral-fluid interface, we see no strong correlation between precipitation rate and boron

910   partitioning or isotopic fractionation compared to aqueous borate ion, unlike in previous

911   work (e.g. Farmer et al., 2019). Our aragonite precipitates – precipitated at or close to

912   predicted oxygen isotope equilibrium (Kim et al. 2014) – support the conclusion of Noireaux

913   et al. (2015) that aragonite records the $\delta^{11}B$ of aqueous borate with negligible fractionation,

914   supporting the use of the boron isotope proxy in e.g. corals for constraining calcifying fluid

915   carbonate chemistry (e.g. McCulloch et al., 2018). In addition, we find that a value of α_B of

916   1.026 (Nir et al., 2015) is more appropriate for use, at least in aragonite. Contrastingly, while

917   our calcite precipitates (and those of Sanyal et al. (2000), remeasured by MC-ICPMS) are

918   closer in $\delta^{11}B$ to borate ion than some previous studies, they still show considerable scatter

919   and are increasingly removed from $\delta^{11}B_{borate}$ at low pH. While at face value this might throw

920   doubt on the application of the proxy in uncalibrated calcites to reconstruct ambient pH, it

921   may be that inorganic precipitation experiments such as these may not be representative of

922   natural conditions. Specifically, experimental designs during precipitation of synthetic

923   calcites have likely driven variable ζ-potentials that are unrepresentative of those seen in

924   biogenic calcites. We put forward two mechanisms by which anomalous patterns could be

925   driven by adsorption electrostatics: either due to the Stark vibrational effect (as suggested

926   by Saldi et al., 2018), or as a result of cation-B pairs exacerbating normally weak kinetic

927   isotope effects. This latter mechanism could also play a role in explaining precipitation rate

928   effects at a constant ζ-potential. While surface complexation modelling, ab initio

929   calculations and precipitation experiments incorporating ζ-potential measurements

930   beyond the scope of this study are required, our data nonetheless advance our

931   understanding of boron incorporation pathways in calcium carbonate, and highlight the

932   importance when addressing this question of considering multiple (possibly interacting)

933   ions, rather than focussing on boron in isolation. In particular, we suggest the provision of

934   binding sites for $B(OH)_4^-$ by Na^+ substitution for Ca^{2+} in the $CaCO_3$ lattice warrants further

935   investigation.

936

952 **Literature cited**

953 Al Mahrouqi D., Vinogradov J. and Jackson M. D. (2016) Temperature dependence of the
954   zeta potential in intact natural carbonates. *Geophys. Res. Lett.* **43**, 11,578-11,587.

955 Al Mahrouqi D., Vinogradov J. and Jackson M. D. (2017) Zeta potential of artificial and
956   natural calcite in aqueous solution. *Adv. Colloid Interface Sci.* **240**, 60–76.

957 Allen K. A. and Hönisch B. (2012) The planktic foraminiferal B/Ca proxy for seawater
958   carbonate chemistry: A critical evaluation. *Earth Planet. Sci. Lett.* **345–348**, 203–211.

959 Allen K. A., Hönisch B., Eggins S. M. and Rosenthal Y. (2012) Environmental controls on B/Ca
960   in calcite tests of the tropical planktic foraminifer species Globigerinoides ruber
961   and Globigerinoides sacculifer. *Earth Planet. Sci. Lett.* **351–352**, 270–280.

962 Amankonah J. O. and Somasundaran P. (1985) Effects of dissolved mineral species on the
963   electrokinetic behavior of calcite and apatite. *Colloids Surf.* **15**, 335–353.

964 Anagnostou E., John E. H., Edgar K. M., Foster G. L., Ridgwell A., Inglis G. N., Pancost R. D.,
965   Lunt D. J. and Pearson P. N. (2016) Changing atmospheric CO2 concentration was
966   the primary driver of early Cenozoic climate. *Nature* **533**, 380–384.

967 Babila T. L., Penman D. E., Hönisch B., Kelly D. C., Bralower T. J., Rosenthal Y. and Zachos J. C.
968   (2018) Capturing the global signature of surface ocean acidification during the
969   Palaeocene–Eocene Thermal Maximum. *Philos. Trans. R. Soc. Math. Phys. Eng. Sci.*
970   **376**, 20170072.

971 Balan E., Noireaux J., Mavromatis V., Saldi G. D., Montouillout V., Blanchard M., Pietrucci F.,
972   Gervais C., Rustad J. R., Schott J. and Gaillardet J. (2018) Theoretical isotopic
973   fractionation between structural boron in carbonates and aqueous boric acid and
974   borate ion. *Geochim. Cosmochim. Acta* **222**, 117–129.

975 Balan E., Pietrucci F., Gervais C., Blanchard M., Schott J. and Gaillardet J. (2016) First-
976   principles study of boron speciation in calcite and aragonite. *Geochim. Cosmochim.*
977   *Acta* **193**, 119–131.

978 Berlin T. S. and Khabakov A. V. (1961) Differences in the electrokinetic potential of
979   carbonate sedimentary rocks of different origin and composition. *Geochemistry* **3**,
980   217–230.

981 Berner R. A. (1975) The role of magnesium in the crystal growth of calcite and aragonite
982   from sea water. *Geochim. Cosmochim. Acta* **39**, 489–504.

983   Branson O. (2018) Boron Incorporation into Marine CaCO3. In *Boron Isotopes* (eds. H.
984   Marschall and G. Foster). Springer International Publishing, Cham. pp. 71–105.
985   Available at: http://link.springer.com/10.1007/978-3-319-64666-4_4 [Accessed
986   April 10, 2018].

987   Branson O., Kaczmarek K., Redfern S. A. T., Misra S., Langer G., Tyliszczak T., Bijma J. and
988   Elderfield H. (2015) The coordination and distribution of B in foraminiferal calcite.
989   *Earth Planet. Sci. Lett.* **416**, 67–72.

990   Busenberg E. and Plummer L. N. (1985) Kinetic and thermodynamic factors controlling the
991   distribution of SO32− and Na+ in calcites and selected aragonites. *Geochim.*
992   *Cosmochim. Acta* **49**, 713–725.

993   Cameron A. C., Gelbach J. B. and Miller D. L. (2008) Bootstrap-Based Improvements for
994   Inference with Clustered Errors. *Rev. Econ. Stat.* **90**, 414–427.

995   Chalk T. B., Hain M. P., Foster G. L., Rohling E. J., Sexton P. F., Badger M. P. S., Cherry S. G.,
996   Hasenfratz A. P., Haug G. H., Jaccard S. L., Martínez-García A., Pälike H., Pancost R. D.
997   and Wilson P. A. (2017) Causes of ice age intensification across the Mid-Pleistocene
998   Transition. *Proc. Natl. Acad. Sci.* **114**, 13114–13119.

999   Charlton S. R. and Parkhurst D. L. (2011a) Modules based on the geochemical model
1000   PHREEQC for use in scripting and programming languages. *Comput. Geosci.* **37**,
1001   1653–1663.

1002 Charlton S. R. and Parkhurst D. L. (2011b) Modules based on the geochemical model
1003   PHREEQC for use in scripting and programming languages. *Comput. Geosci.* **37**,
1004   1653–1663.

1005 Cicerone D. S., Regazzoni A. E. and Blesa M. A. (1992) Electrokinetic properties of the
1006   calcite/water interface in the presence of magnesium and organic matter. *J. Colloid*
1007   *Interface Sci.* **154**, 423–433.

1008 Cusack M., Kamenos N. A., Rollion-Bard C. and Tricot G. (2015) Red coralline algae assessed
1009   as marine pH proxies using 11B MAS NMR. *Sci. Rep.* **5**. Available at:
1010   http://www.nature.com/articles/srep08175 [Accessed April 10, 2018].

1011 Davies C. W. (1938) 397. The extent of dissociation of salts in water. Part VIII. An equation
1012   for the mean ionic activity coefficient of an electrolyte in water, and a revision of
1013   the dissociation constants of some sulphates. *J. Chem. Soc. Resumed*, 2093.

1014 De Groot K. and Duyvis E. M. (1966) Crystal Form of Precipitated Calcium Carbonate as
1015   influenced by Adsorbed Magnesium Ions. *Nature* **212**, 183–184.

1016 DePaolo D. J. (2011) Surface kinetic model for isotopic and trace element fractionation
1017   during precipitation of calcite from aqueous solutions. *Geochim. Cosmochim. Acta*
1018   **75**, 1039–1056.

1019 Dickson A. G. (1990a) Oceanographic Research Papers : Thermodynamics of the
1020   dissociation of boric acid in synthetic seawater from 273.15 to 318.15 K. *Deep Sea*
1021   *Res. Part A* **37**, 755–766.

1022 Dickson A. G. (1990b) Thermodynamics of the dissociation of boric acid in potassium
1023   chloride solutions from 273.15 to 318.15 K. *J. Chem. Eng. Data* **35**, 253–257.

Douglas H. W. and Walker R. A. (1950) The electrokinetic behaviour of iceland spar against aqueous electrolyte solutions. *Trans. Faraday Soc.* **46**, 559.

Dove P. M., de Yoreo J. J. and Davis K. J. (2004) Inhibition of CaCO3 crystallization by small molecules: the magnesium example. In *Nannoscale structure and assembly at solid-fluid interfaces, volume II: Assembly in Hybrid and Biological Systems* Kluwer Academic Publishers, Dordecht, Netherlands. pp. 56–82.

Epstein S. and Mayeda T. (1953) Variation of O18 content of waters from natural sources. *Geochim. Cosmochim. Acta* **4**, 213–224.

Evans D., Gray W. R., Rae J. W. B., Greenop R., Webb P. B., Penkman K., Kröger R. and Allison N. (2020) Trace and major element incorporation into amorphous calcium carbonate (ACC) precipitated from seawater. *Geochim. Cosmochim. Acta* **290**, 293–311.

Farmer J. R., Branson O., Uchikawa J., Penman D. E., Hönisch B. and Zeebe R. E. (2019) Boric acid and borate incorporation in inorganic calcite inferred from B/Ca, boron isotopes and surface kinetic modeling. *Geochim. Cosmochim. Acta* **244**, 229–247.

Farmer J. R., Hönisch B. and Uchikawa J. (2016) Single laboratory comparison of MC-ICP-MS and N-TIMS boron isotope analyses in marine carbonates. *Chem. Geol.* **447**, 173–182.

Fenter P., Geissbühler P., DiMasi E., Srajer G., Sorensen L. B. and Sturchio N. C. (2000) Surface speciation of calcite observed in situ by high-resolution X-ray reflectivity. *Geochim. Cosmochim. Acta* **64**, 1221–1228.

Fenter P. and Sturchio N. C. (2004) Mineral–water interfacial structures revealed by synchrotron X-ray scattering. *Prog. Surf. Sci.* **77**, 171–258.

Foster G. L. (2008) Seawater pH, pCO$_2$ and [CO$_3^{2-}$] variations in the Caribbean Sea over the last 130kyr: A boron isotope and B/Ca study of planktic foraminifera. *Earth Planet. Sci. Lett.* **271**, 254–266.

Foster G. L., Hönisch B., Paris G., Dwyer G. S., Rae J. W. B., Elliott T. R., Gaillardet J., Hemming N. G., Louvat P. and Vengosh A. (2013) Interlaboratory comparison of boron isotope analyses of boric acid, seawater and marine CaCO3 by MC-ICPMS and NTIMS. *Chem. Geol.* **358**, 1–14.

Foster G. L. and Rae J. W. B. (2016) Reconstructing Ocean pH with Boron Isotopes in Foraminifera. *Annu. Rev. Earth Planet. Sci.* **44**, 207–237.

Foster G. L., Strandmann P. A. E. P. von and Rae J. W. B. (2010) Boron and magnesium isotopic composition of seawater. *Geochem. Geophys. Geosystems* **11**, 10 PP.

Foxall T., Peterson G. C., Rendall H. M. and Smith A. L. (1979) Charge determination at calcium salt/aqueous solution interface. *J. Chem. Soc. Faraday Trans. 1 Phys. Chem. Condens. Phases* **75**, 1034.

Füger A., Konrad F., Leis A., Dietzel M. and Mavromatis V. (2019) Effect of growth rate and pH on lithium incorporation in calcite. *Geochim. Cosmochim. Acta* **248**, 14–24.

1063   Furst M., Lowenstam H. A. and Burnett D. S. (1976) Radiographic study of the distribution of
1064   boron in recent mollusc shells. *Geochim. Cosmochim. Acta* **40**, 1381–1386.

1065   Gabitov R. I., Gaetani G. A., Watson E. B., Cohen A. L. and Ehrlich H. L. (2008) Experimental
1066   determination of growth rate effect on U6+ and Mg2+ partitioning between
1067   aragonite and fluid at elevated U6+ concentration. *Geochim. Cosmochim. Acta* **72**,
1068   4058–4068.

1069   Gagnon A. C., Gothmann A. M., Branson O., Rae J. W. B. and Stewart J. A. (2021) Controls on
1070   boron isotopes in a cold-water coral and the cost of resilience to ocean
1071   acidification. *Earth Planet. Sci. Lett.* **554**, 116662.

1072   Geissbühler P., Fenter P., DiMasi E., Srajer G., Sorensen L. B. and Sturchio N. C. (2004) Three-
1073   dimensional structure of the calcite–water interface by surface X-ray scattering.
1074   *Surf. Sci.* **573**, 191–203.

1075   Glover P. W. J., Walker E. and Jackson M. D. (2012) Streaming-potential coefficient of
1076   reservoir rock: A theoretical model. *GEOPHYSICS* **77**, D17–D43.

1077   Goldberg S. and Forster H. S. (1991) Boron sorption on calcareous soils and reference
1078   calcites. *Soil Sci.* **152**, 304–310.

1079   Hain M. P., Sigman D. M., Higgins J. A. and Haug G. H. (2015) The effects of secular calcium
1080   and magnesium concentration changes on the thermodynamics of seawater
1081   acid/base chemistry: Implications for Eocene and Cretaceous ocean carbon
1082   chemistry and buffering. *Glob. Biogeochem. Cycles*, 2014GB004986.

1083   Heberling F., Trainor T. P., Lützenkirchen J., Eng P., Denecke M. A. and Bosbach D. (2011)
1084   Structure and reactivity of the calcite–water interface. *J. Colloid Interface Sci.* **354**,
1085   843–857.

1086   Hemming N. G. and Hanson G. N. (1992) Boron isotopic composition and concentration in
1087   modern marine carbonates. *Geochim. Cosmochim. Acta* **56**, 537–543.

1088   Henehan M. J., Edgar K. M., Foster G. L., Penman D. E., Hull P. M., Greenop R., Anagnostou E.
1089   and Pearson P. N. (2020) Revisiting the Middle Eocene Climatic Optimum 'Carbon
1090   Cycle Conundrum' with new estimates of atmospheric pCO$_2$ from boron isotopes.
1091   *Paleoceanogr. Paleoclimatology* **35**, e2019PA003713.

1092   Henehan M. J., Foster G. L., Rae J. W. B., Prentice K. C., Erez J., Bostock H. C., Marshall B. J.
1093   and Wilson P. A. (2015) Evaluating the utility of B/Ca ratios in planktic foraminifera
1094   as a proxy for the carbonate system: A case study of *Globigerinoides ruber*:
1095   Investigating controls on *G. ruber* B/Ca. *Geochem. Geophys. Geosystems* **16**, 1052–
1096   1069.

1097   Henehan M. J., Rae J. W. B., Foster G. L., Erez J., Prentice K. C., Kucera M., Bostock H. C.,
1098   Martínez-Botí M. A., Milton J. A., Wilson P. A., Marshall B. J. and Elliott T. (2013)
1099   Calibration of the boron isotope proxy in the planktonic foraminifera
1100   Globigerinoides ruber for use in palaeo-CO$_2$ reconstruction. *Earth Planet. Sci. Lett.*
1101   **364**, 111–122.

1102 Hershey J. P., Fernandez M., Milne P. J. and Millero F. J. (1986) The ionization of boric acid in
1103   NaCl, Na-Ca-Cl and Na-Mg-Cl solutions at 25°C. *Geochim. Cosmochim. Acta* **50**, 143–
1104   148.

1105 Holcomb M., DeCarlo T. M., Gaetani G. A. and McCulloch M. (2016) Factors affecting B/Ca
1106   ratios in synthetic aragonite. *Chem. Geol.* **437**, 67–76.

1107 Holcomb M., Venn A. A., Tambutté E., Tambutté S., Allemand D., Trotter J. and McCulloch
1108   M. (2014) Coral calcifying fluid pH dictates response to ocean acidification. *Sci. Rep.*
1109   **4**. Available at: http://www.nature.com/articles/srep05207 [Accessed May 4, 2020].

1110 Hönisch B., Bijma J., Russell A. D., Spero H. J., Palmer M. R., Zeebe R. E. and Eisenhauer A.
1111   (2003) The influence of symbiont photosynthesis on the boron isotopic
1112   composition of foraminifera shells. *Mar. Micropaleontol.* **49**, 87–96.

1113 Hönisch B., Eggins S., Haynes L. L., Allen K. A., Holland K. D. and Lorbacher K. (2019) *Boron*
1114   *proxies in paleoceanography and paleoclimatology*., Wiley Blackwell, Hoboken, NJ.

1115 Imbens G. W. and Kolesar M. (2012) *Robust Standard Errors in Small Samples: Some Practical*
1116   *Advice*., National Bureau of Economic Research. Available at:
1117   http://www.nber.org/papers/w18478 [Accessed January 24, 2016].

1118 Kaczmarek K., Nehrke G., Misra S., Bijma J. and Elderfield H. (2016a) Investigating the effects
1119   of growth rate and temperature on the B/Ca ratio and δ11B during inorganic
1120   calcite formation. *Chem. Geol.* **421**, 81–92.

1121 Kaczmarek K., Nehrke G., Misra S., Bijma J. and Elderfield H. (2016b) Investigating the
1122   effects of growth rate and temperature on the B/Ca ratio and δ11B during
1123   inorganic calcite formation. *Chem. Geol.* **421**, 81–92.

1124 Kester D. R., Duedall I. W., Connors D. N. and Pytkowicz R. M. (1967) PREPARATION OF
1125   ARTIFICIAL SEAWATER1. *Limnol. Oceanogr.* **12**, 176–179.

1126 Kim S.-T., Gebbinck C. K., Mucci A. and Coplen T. B. (2014) Oxygen isotope systematics in
1127   the aragonite–CO2–H2O–NaCl system up to 0.7 mol/kg ionic strength at 25 °C.
1128   *Geochim. Cosmochim. Acta* **137**, 147–158.

1129 Kim S.-T., Hillaire-Marcel C. and Mucci A. (2006) Mechanisms of equilibrium and kinetic
1130   oxygen isotope effects in synthetic aragonite at 25 °C. *Geochim. Cosmochim. Acta*
1131   **70**, 5790–5801.

1132 Kim S.-T. and O'Neil J. R. (1997) Equilibrium and nonequilibrium oxygen isotope effects in
1133   synthetic carbonates. *Geochim. Cosmochim. Acta* **61**, 3461–3475.

1134 Kitano Y., Okumura M. and Idogaki M. (1975) Incorporation of sodium, chloride and sulfate
1135   with calcium carbonate. *Geochem. J.* **9**, 75–84.

1136 Kitano Y., Okumura Y. M. and Idogaki M. (1978) Coprecipitation of borate-boron with
1137   calcium carbonate. *Geochem. J.* **12**, 183–189.

1138 Klochko K., Cody G. D., Tossell J. A., Dera P. and Kaufman A. J. (2009) Re-evaluating boron
1139   speciation in biogenic calcite and aragonite using 11B MAS NMR. *Geochim.*
1140   *Cosmochim. Acta* **73**, 1890–1900.

1141 Klochko K., Kaufman A. J., Yao W., Byrne R. H. and Tossell J. A. (2006) Experimental
1142   measurement of boron isotope fractionation in seawater. *Earth Planet. Sci. Lett.*
1143   **248**, 276–285.

1144 Lambert D. K. (1996) Vibrational Stark effect of adsorbates at electrochemical interfaces.
1145   *Electrochimica Acta* **41**, 623–630.

1146 Liu R. Y. (1988) Bootstrap procedures under some non-iid models. *Ann. Stat.* **16**, 1696–
1147   1708.

1148 Mammen E. (1993) Bootstrap and Wild Bootstrap for High Dimensional Linear Models. *Ann.*
1149   *Stat.* **21**, 255–285.

1150 Martínez-Botí M. A., Foster G. L., Chalk T. B., Rohling E. J., Sexton P. F., Lunt D. J., Pancost R.
1151   D., Badger M. P. S. and Schmidt D. N. (2015) Plio-Pleistocene climate sensitivity
1152   evaluated using high-resolution CO2 records. *Nature* **518**, 49–54.

1153 Mavromatis V., Gautier Q., Bosc O. and Schott J. (2013) Kinetics of Mg partition and Mg
1154   stable isotope fractionation during its incorporation in calcite. *Geochim.*
1155   *Cosmochim. Acta* **114**, 188–203.

1156 Mavromatis V., Montouillout V., Noireaux J., Gaillardet J. and Schott J. (2015)
1157   Characterization of boron incorporation and speciation in calcite and aragonite
1158   from co-precipitation experiments under controlled pH, temperature and
1159   precipitation rate. *Geochim. Cosmochim. Acta* **150**, 299–313.

1160 McCulloch M., Falter J., Trotter J. and Montagna P. (2012) Coral resilience to ocean
1161   acidification and global warming through pH up-regulation. *Nat. Clim. Change* **2**,
1162   623–627.

1163 McCulloch M. T., D'Olivo J. P., Falter J., Georgiou L., Holcomb M., Montagna P. and Trotter J.
1164   A. (2018) Boron Isotopic Systematics in Scleractinian Corals and the Role of pH Up-
1165   regulation. In *Boron Isotopes* (eds. H. Marschall and G. Foster). Advances in Isotope
1166   Geochemistry. Springer International Publishing, Cham. pp. 145–162. Available at:
1167   http://link.springer.com/10.1007/978-3-319-64666-4_6 [Accessed April 24, 2020].

1168 Millero F. J. and Pierrot D. (1998) A Chemical Equilibrium Model for Natural Waters. *Aquat.*
1169   *Geochem.* **4**, 153–199.

1170 Morse J. W., Arvidson R. S. and Lüttge A. (2007) Calcium Carbonate Formation and
1171   Dissolution. *Chem. Rev.* **107**, 342–381.

1172 Moulin P. and Roques H. (2003) Zeta potential measurement of calcium carbonate. *J.*
1173   *Colloid Interface Sci.* **261**, 115–126.

1174 Mucci A. (1988) Manganese uptake during calcite precipitation from seawater: Conditions
1175   leading to the formation of a pseudokutnahorite. *Geochim. Cosmochim. Acta* **52**,
1176   1859–1868.

1177 Mucci A. and Morse J. W. (1983) The incorporation of Mg2+ and Sr2+ into calcite
1178   overgrowths: influences of growth rate and solution composition. *Geochim.*
1179   *Cosmochim. Acta* **47**, 217–233.

1180   Nehrke G., Reichart G. J., Van Cappellen P., Meile C. and Bijma J. (2007) Dependence of
1181   calcite growth rate and Sr partitioning on solution stoichiometry: Non-Kossel
1182   crystal growth. *Geochim. Cosmochim. Acta* **71**, 2240–2249.

1183   Nielsen M. R., Sand K. K., Rodriguez-Blanco J. D., Bovet N., Generosi J., Dalby K. N. and Stipp
1184   S. L. S. (2016) Inhibition of Calcite Growth: Combined Effects of Mg $^{2+}$ and SO $_4$ $^{2-}$.
1185   *Cryst. Growth Des.* **16**, 6199–6207.

1186   Nir O., Marvin E. and Lahav O. (2014) Accurate and self-consistent procedure for
1187   determining pH in seawater desalination brines and its manifestation in reverse
1188   osmosis modeling. *Water Res.* **64**, 187–195.

1189   Nir O., Vengosh A., Harkness J. S., Dwyer G. S. and Lahav O. (2015) Direct measurement of
1190   the boron isotope fractionation factor: Reducing the uncertainty in reconstructing
1191   ocean paleo-pH. *Earth Planet. Sci. Lett.* **414**, 1–5.

1192   Noireaux J., Mavromatis V., Gaillardet J., Schott J., Montouillout V., Louvat P., Rollion-Bard C.
1193   and Neuville D. R. (2015) Crystallographic control on the boron isotope paleo-pH
1194   proxy. *Earth Planet. Sci. Lett.* **430**, 398–407.

1195   Okai T., Suzuki A., Kawahata H., Terashima S. and Imai N. (2002) Preparation of a New
1196   Geological Survey of Japan Geochemical Reference Material: Coral JCp-1. *Geostand.*
1197   *Newsl.* **26**, 95–99.

1198   Owen B. B. and King E. J. (1943) The Effect of Sodium Chloride upon the Ionization of Boric
1199   Acid at Various Temperatures [1]. *J. Am. Chem. Soc.* **65**, 1612–1620.

1200   Parkhurst D. L. and Appelo C. A. J. (2013) *Description of input and examples for PHREEQC*
1201   *version 3: a computer program for speciation, batch-reaction, one-dimensional*
1202   *transport, and inverse geochemical calculations.*, US Geological Society. Available at:
1203   http://pubs.usgs.gov/tm/06/a43.

1204   Penman D. E., Hönisch B., Zeebe R. E., Thomas E. and Zachos J. C. (2014) Rapid and
1205   sustained surface ocean acidification during the Paleocene-Eocene Thermal
1206   Maximum. *Paleoceanography*, 2014PA002621.

1207   Rae J. W. B. (2018) Boron Isotopes in Foraminifera: Systematics, Biomineralisation, and CO2
1208   Reconstruction. In *Boron Isotopes* (eds. H. Marschall and G. Foster). Advances in
1209   Isotope Geochemistry. Springer International Publishing, Cham. pp. 107–143.
1210   Available at: http://link.springer.com/10.1007/978-3-319-64666-4_5 [Accessed
1211   March 30, 2020].

1212   Ruiz-Agudo E., Putnis C. V., Kowacz M., Ortega-Huertas M. and Putnis A. (2012) Boron
1213   incorporation into calcite during growth: Implications for the use of boron in
1214   carbonates as a pH proxy. *Earth Planet. Sci. Lett.* **345–348**, 9–17.

1215   Saldi G. D., Noireaux J., Louvat P., Faure L., Balan E., Schott J. and Gaillardet J. (2018) Boron
1216   isotopic fractionation during adsorption by calcite – Implication for the seawater
1217   pH proxy. *Geochim. Cosmochim. Acta* **240**, 255–273.

1218   Sanyal A., Nugent M., Reeder R. J. and Bijma J. (2000) Seawater pH control on the boron
1219   isotopic composition of calcite: evidence from inorganic calcite precipitation
1220   experiments. *Geochim. Cosmochim. Acta* **64**, 1551–1555.

1221   Schindler P. W. and Stumm W. (1987) The surface chemistry of oxides, hydroxides, and
1222   oxide minerals. In *Aquatic Surface Chemistry: Chemical Processes at the Particle-*
1223   *Water Interface* (ed. W. Stumm). John Wiley & Sons, New York. pp. 83–110.

1224   Schoepf V., Jury C. P., Toonen R. J. and McCulloch M. T. (2017) Coral calcification
1225   mechanisms facilitate adaptive responses to ocean acidification. *Proc. R. Soc. B Biol.*
1226   *Sci.* **284**, 20172117.

1227   SciPy 1.0 Contributors, Virtanen P., Gommers R., Oliphant T. E., Haberland M., Reddy T.,
1228   Cournapeau D., Burovski E., Peterson P., Weckesser W., Bright J., van der Walt S. J.,
1229   Brett M., Wilson J., Millman K. J., Mayorov N., Nelson A. R. J., Jones E., Kern R., Larson
1230   E., Carey C. J., Polat İ., Feng Y., Moore E. W., VanderPlas J., Laxalde D., Perktold J.,
1231   Cimrman R., Henriksen I., Quintero E. A., Harris C. R., Archibald A. M., Ribeiro A. H.,
1232   Pedregosa F. and van Mulbregt P. (2020) SciPy 1.0: fundamental algorithms for
1233   scientific computing in Python. *Nat. Methods* **17**, 261–272.

1234   Sen S., Stebbins J. F., Hemming N. G. and Ghosh B. (1994) Coordination environments of B
1235   impurities in calcite and aragonite polymorphs; A 11 B MAS NMR study. *Am.*
1236   *Mineral.* **79**, 819–825.

1237   Siffert D. and Fimbel P. (1984) Parameters affecting the sign and magnitude of the
1238   eletrokinetic potential of calcite. *Colloids Surf.* **11**, 377–389.

1239   Smallwood P. V. (1977) Some aspects of the surface chemistry of calcite and aragonite Part
1240   I: An electrokinetic study. *Colloid Polym. Sci.* **255**, 881–886.

1241   Stipp S. L. S. (1999) Toward a conceptual model of the calcite surface: hydration, hydrolysis,
1242   and surface potential. *Geochim. Cosmochim. Acta* **63**, 3121–3131.

1243   Uchikawa J., Harper D. T., Penman D. E., Zachos J. C. and Zeebe R. E. (2017) Influence of
1244   solution chemistry on the boron content in inorganic calcite grown in artificial
1245   seawater. *Geochim. Cosmochim. Acta* **218**, 291–307.

1246   Uchikawa J., Penman D. E., Zachos J. C. and Zeebe R. E. (2015) Experimental evidence for
1247   kinetic effects on B/Ca in synthetic calcite: Implications for potential B(OH)4− and
1248   B(OH)3 incorporation. *Geochim. Cosmochim. Acta* **150**, 171–191.

1249   Vdović N. (2001) Electrokinetic behaviour of calcite—the relationship with other calcite
1250   properties. *Chem. Geol.* **177**, 241–248.

1251   Venn A. A., Tambutte E., Holcomb M., Laurent J., Allemand D. and Tambutte S. (2013)
1252   Impact of seawater acidification on pH at the tissue-skeleton interface and
1253   calcification in reef corals. *Proc. Natl. Acad. Sci.* **110**, 1634–1639.

1254   Wang Y.-J., Wei H.-Z., Jiang S.-Y., van de Ven T. G. M., Ling B.-P., Li Y.-C., Lin Y.-B. and Guo Q.
1255   (2018) Mechanism of boron incorporation into calcites and associated isotope
1256   fractionation in a steady-state carbonate-seawater system. *Appl. Geochem.* **98**,
1257   221–236.

1258   Watson E. B. (2004) A conceptual model for near-surface kinetic controls on the trace-
1259   element and stable isotope composition of abiogenic calcite crystals. *Geochim.*
1260   *Cosmochim. Acta* **68**, 1473–1488.

1261   van der Weijden C. H. and van der Weijden R. D. (2014) Calcite growth: Rate dependence
1262   on saturation, on ratios of dissolved calcium and (bi)carbonate and on their
1263   complexes. *J. Cryst. Growth* **394**, 137–144.

1264   Wolthers M., Charlet L. and Van Cappellen P. (2008) The surface chemistry of divalent metal
1265   carbonate minerals; a critical assessment of surface charge and potential data
1266   using the charge distribution multi-site ion complexation model. *Am. J. Sci.* **308**,
1267   905–941.

1268   Yoshimura T., Tamenori Y., Suzuki A., Kawahata H., Iwasaki N., Hasegawa H., Nguyen L. T.,
1269   Kuroyanagi A., Yamazaki T., Kuroda J. and Ohkouchi N. (2017) Altervalent
1270   substitution of sodium for calcium in biogenic calcite and aragonite. *Geochim.*
1271   *Cosmochim. Acta* **202**, 21–38.

1272   Yu J., Day J., Greaves M. and Elderfield H. (2005) Determination of multiple
1273   element/calcium ratios in foraminiferal calcite by quadrupole ICP-MS. *Geochem.*
1274   *Geophys. Geosystems* **6**, Q08P01.

1275   Zeebe R. E., Sanyal A., Ortiz J. D. and Wolf-Gladrow D. (2001) A theoretical study of the
1276   kinetics of the boric acid–borate equilibrium in seawater. *Mar. Chem.* **73**, 113–124.

1277   Zeebe R. E. and Wolf-Gladrow D. A. (2001) *CO2 in seawater: Equilibrium, Kinetics, Isotopes.*,
1278   Elsevier, Amsterdam.

1279   Zhang J. and Nancollas G. H. (1998) Kink Density and Rate of Step Movement during
1280   Growth and Dissolution of anABCrystal in a Nonstoichiometric Solution. *J. Colloid*
1281   *Interface Sci.* **200**, 131–145.

1282

Table 1: Precipitation conditions and chemistry of growth media. Note, experiments were unseeded: the polymorph precipitated in each case was determined only by the ratio of Mg to Ca in the growth solutions. XRD analysis confirmed purity of polymorph in each case.

Sample name	Polymorph	Reactor volume (L)	Duration (hrs)	Mass precipitated (mg)	Precipitation rate (mg/hr)	pH (NBS scale) mean	2sd	2se	Starting Growth Medium Values NaHCO$_3$ (mMol/kgw)	Na$_2$CO$_3$ (mMol/kgw)	Ca (mMol/kgw)	Mg (mMol/kgw)	B (mMol/kgw)	NaCl (mMol/kgw)	Titrant 1 NaHCO$_3$ (mMol/kgw)	Na$_2$CO$_3$ (mMol/kgw)	NaCl (mMol/kgw)	Titrant 2 Ca (mMol/kgw)	B (mMol/kgw)	NaCl (mMol/kgw)	Amount of Titrants added (L)
CKG-Oct511	Aragonite	1	375.2	70.01	0.187	8.765	0.061	0.016	5	5	0.5	2	7.9	685	60	20	620	3	20	695	0.19
iMH1 / 1-Mar2112-C	Aragonite	1	411.1	45.33	0.110	8.780	0.049	0.014	5	5	0.5	2	7.9	685	60	20	620	3	20	695	0.21
iMH2 / 1-Apr2712-D	Aragonite	1	405.9	42.67	0.105	8.830	0.079	0.024	5	5	0.5	2	7.9	685	60	20	620	5	20	695	0.20
iMH3 / 1-Aug312-D2	Aragonite	2	406.9	263.51	0.648	9.326	0.099	0.018	0	10	0.25	1	7.9	685	0	80	510	3	20	695	0.20
iMH4 / 1-Aug3012-E	Aragonite	2	626.9	79.34	0.127	8.762	0.084	0.017	5	5	0.5	2	7.9	685	60	20	620	5	20	695	0.31
iMH5 / 1-Sept2512-D2	Aragonite	2	595.2	92.44	0.155	9.376	0.053	0.009	0	10	0.25	1	7.9	685	0	80	510	3	20	695	0.30
iMH6 / 1-Oct2912-E	Aragonite	2	595.2	71.39	0.120	8.717	0.046	0.010	5	5	0.5	2	7.9	685	60	20	620	5	20	695	0.30
iMH7 / DEC512_D2	Aragonite	2	479.4	67.07	0.140	9.408	0.102	0.021	0	10	0.25	1	7.9	685	0	80	510	5	20	695	0.24
iMH8 / FEB2513_C	Aragonite	2	450.8	75.21	0.167	9.425	0.110	0.022	0	10	0.25	1	7.9	685	0	80	510	5	20	695	0.23
iMH9 / FEB2513_D	Aragonite	2	450.8	58.76	0.130	9.431	0.108	0.022	0	10	0.25	1	7.9	685	0	80	510	5	20	695	0.23
iMH10 / FEB2513_E	Aragonite	2	283.0	389.06	1.375	7.452	0.246	0.066	10	0	10	40	7.9	570	60	20	620	10	20	695	0.14
iMH11 / APR313_C	Aragonite	2	307.3	339.86	1.106	7.590	0.281	0.072	10	0	10	40	7.9	570	60	20	620	10	20	695	0.15
iMH12 / APR313_D	Aragonite	2	211.6	334.98	1.583	7.562	0.228	0.066	10	0	10	40	7.9	570	60	20	620	10	20	695	0.11
iMH13 / APR313_E	Aragonite	2	67.2	67.00	0.997	7.601	0.256	0.105	10	0	10	40	7.9	570	60	20	620	3	20	695	0.03
iMH14 / OCT2912_E2	Aragonite	2	599.7	88.08	0.147	8.686	0.052	0.011	5	5	0.5	2	7.9	685	60	20	620	5	20	695	0.30
iMH15 / DEC512_D	Aragonite	2	599.7	79.85	0.133	9.337	0.127	0.023	0	10	0.25	1	7.9	685	0	80	510	10	20	695	0.30
iMH16 / DEC1412_C	Aragonite	2	599.7	270.13	0.450	7.535	0.158	0.026	7.5	2.5	10	40	7.9	592	16	4	685	10	20	695	0.30
iMH17 / 0628C-MRS1	Calcite	2	358.5	100.00	0.279	8.400	0.244	0.063	7.5	2.5	1	0.13	7.9	692	16	4	685	10	20	685	0.18
iMH18 / 0628D-MRS1	Calcite	2	358.5	92.00	0.257	8.580	0.149	0.039	7.5	2.5	1	0.13	7.9	692	16	4	685	10	20	685	0.18
iMH19 / 0628E-MRS1	Calcite	2	358.5	110.00	0.307	8.700	0.247	0.064	7.5	2.5	1	0.13	7.9	692	16	4	685	10	20	685	0.18
iMH20 / 0730D-MRS1	Calcite	2	594.8	91.00	0.153	8.460	0.068	0.015	7.5	2.5	1	0.13	7.9	692	16	4	685	10	20	685	0.30
iMH21 / 0730E-MRS1	Calcite	2	594.8	113.00	0.190	8.420	0.151	0.032	7.5	2.5	1	0.13	7.9	692	16	4	685	10	20	685	0.30
iMH23 / 1112A-MRSI	Calcite	2	452.2	330.00	0.730	7.400	0.242	0.061	10.0	0.0	10	1.30	7.9	673	20	0	690	10	20	685	0.23
iMH24 / 1112C-MRSI	Calcite	2	452.2	325.00	0.719	7.430	0.231	0.058	10.0	0.0	10	1.30	7.9	673	20	0	690	10	20	685	0.23
iMH25 / 1204A-MRSI	Calcite	2	385.3	212.00	0.550	7.460	0.208	0.054	10.0	0.0	10	1.30	7.9	673	20	0	690	10	20	685	0.19
iMH26 / 1204C-MRSI	Calcite	2	385.3	188.00	0.488	7.460	0.195	0.050	10.0	0.0	10	1.30	7.9	673	20	0	690	10	20	685	0.19

Sample name	Polymorph	pH (NBS scale) mean	2se	Carbonate Oxygen Isotope Fractionation 1000lnα (‰)	±1σ	B/Ca µmol/mol	Carbonate Na/Ca mmol/mol	Mg/Ca mmol/mol	Carbonate δ11B (‰)	Ext. rep. (‰, 2sd)	Starting Solution δ11B (‰)	Ext. rep. (‰, 2sd)	End Solution δ11B (‰)	Ext. rep. (‰, 2sd)	Carbonate normalised to sw = 39.61 ‰ δ11B (‰)
CKG-Oct511	Aragonite	8.765	0.016	28.99	0.09	1061	19.875	1.197	-28.36	0.18			-14.39	0.18	24.83
iMH1 / 1-Mar2112-C	Aragonite	8.780	0.014	28.92	0.09	1174	21.515	1.240	-28.58	0.19	-14.31	0.22	-14.40	0.22	24.60
iMH2 / 1-Apr2712-D	Aragonite	8.830	0.024	28.92	0.09	1187	22.114	1.319	-28.70	0.19	-14.21	0.22	-14.35	0.22	24.47
iMH3 / 1-Aug312-D2	Aragonite	9.326	0.018	29.09	0.09	1858	21.885	6.035	-22.28	0.17	-14.45	0.22	-14.48	0.22	31.24
iMH4 / 1-Aug3012-E	Aragonite	8.762	0.017	28.90	0.09	750	16.018	1.034	-28.74	0.20	-14.33	0.22	-14.49	0.22	24.43
iMH5 / 1-Sept2512-D2	Aragonite	9.376	0.009	28.88	0.09	1077	20.985	2.388	-19.50	0.17	-14.30	0.22	-14.33	0.22	34.17
iMH6 / 1-Oct2912-E	Aragonite	8.717	0.010	28.84	0.09	1314	23.111	1.307	-28.54	0.18	-14.35	0.22	-14.35	0.20	24.63
iMH7 / DEC512_D2	Aragonite	9.408	0.021	28.89	0.09	969	18.130	2.525	-18.99	0.18					34.71
iMH8 / FEB2513_C	Aragonite	9.425	0.022	29.02	0.09	1048	19.517	1.994	-18.85	0.19	-14.25	0.16			34.86
iMH9 / FEB2513_D	Aragonite	9.431	0.022	28.97	0.09	1477	27.365	3.656	-18.96	0.19					34.74
iMH10 / FEB2513_E	Aragonite	7.452	0.066	29.08	0.09	349	7.953	1.008	-38.53	0.26					14.10
iMH11 / APR313_C	Aragonite	7.590	0.072	29.10	0.09	912	13.968	1.412	-37.90	0.19	-14.35	0.19	-14.33	0.19	14.77
iMH12 / APR313_D	Aragonite	7.562	0.066	29.05	0.09	695	11.308	0.976	-38.06	0.19					14.59
iMH13 / APR313_E	Aragonite	7.601	0.105	29.01	0.09	1406	16.817	2.029	-37.99	0.19					14.67
iMH14 / OCT2912_E2	Aragonite	8.686	0.011	28.80	0.09	862	17.128	1.654	-28.68	0.20					24.48
iMH15 / DEC512_D	Aragonite	9.337	0.023	28.84	0.09	1110	22.446	3.614	-19.00	0.19	-14.51	0.20			34.70
iMH16 / DEC1412_C	Aragonite	7.535	0.026	29.15	0.09	617	8.139	1.091	-37.28	0.21					15.42
iMH17 / 0628C-MRS1	Calcite	8.400	0.063	28.44	0.09	168	3.714	4.345	-31.01	0.25	-14.31	0.20			22.03
iMH18 / 0628D-MRS1	Calcite	8.580	0.039	28.53	0.09	298	3.695	2.979	-31.70	0.22			-14.28	0.19	21.30
iMH19 / 0628E-MRS1	Calcite	8.700	0.064	28.49	0.09	246	3.476	4.728	-30.13	0.21			-14.24	0.19	22.96
iMH20 / 0730D-MRS1	Calcite	8.460	0.015	28.42	0.09	267	3.465	2.428	-31.10	0.21	-14.27	0.20			21.94
iMH21 / 0730E-MRS1	Calcite	8.420	0.032	28.59	0.09	171	2.778	4.521	-29.71	0.22			-14.27	0.20	23.39
iMH23 / 1112A-MRSI	Calcite	7.400	0.061	28.66	0.09	117	1.391	4.728	-34.60	0.23			-14.29	0.19	18.25
iMH24 / 1112C-MRSI	Calcite	7.430	0.058	28.73	0.09	126	1.365	4.697	-34.78	0.21	-14.29	0.19			18.06
iMH25 / 1204A-MRSI	Calcite	7.460	0.054	28.59	0.09	109	1.385	4.617	-34.49	0.22	-14.27	0.20			18.36
iMH26 / 1204C-MRSI	Calcite	7.460	0.050	28.66	0.09	112	1.294	4.545	-34.83	0.26			-14.27	0.16	18.00

Table 2: Measured carbonate oxygen isotope fractionation, El/Ca ratios and δ11B, and measured growth medium δ11B. Note, since we see no evidence of any isotopic fractionation outside of uncertainty during experiments, or variability between experiments, we did not measure every growth medium solution before and after precipitation. Rather, we take the mean and 2se of all growth medium δ11B measurements as the parent solution value (and associated uncertainty) for all carbonates. Uncertainty on B/Ca measurements is 6%, and for Mg/Ca and Na/Ca is 2%, based on repeat measurements of in-house standards during the relevant analytical runs.